

**DESIGN AND CONSTRUCTION OF A DEPOSITION CHAMBER
FOR THIN METAL FILMS RESEARCH**

By

Kurt M. Aikens

A thesis submitted in partial fulfillment of the requirements for the degree of

Bachelor of Science

Houghton College

May 2009

Signature of Author.....

Department of Physics
May 6, 2009

.....

Dr. Brandon Hoffman
Assistant Professor of Physics
Research Supervisor

.....

Dr. Mark Yuly
Professor of Physics

DESIGN AND CONSTRUCTION OF A DEPOSITION CHAMBER FOR THIN METAL FILMS RESEARCH

By

Kurt M. Aikens

Submitted to the Houghton College Department of Physics
on May 6, 2009 in partial fulfillment of the
requirement for the degree of
Bachelor of Science

Abstract

A high vacuum deposition chamber is being built at Houghton College for the production and study of thin metal films. Up to four electron-beam heated crucibles will be used to evaporate metals whose evaporate is adsorbed onto a substrate, forming a film. Evaporation rates may be monitored via crucible temperatures or direct measurement of the ionized flux. The chamber will feature a computer-controlled shield enabling the deposition of samples with varying thickness gradients and an ion gun for substrate cleaning and ion beam assisted deposition (IBAD). The history and theory of vacuum and deposition technologies are discussed. Future plans and current progress are also presented.

Thesis Supervisor: Dr. Brandon Hoffman
Title: Assistant Professor of Physics

TABLE OF CONTENTS

Chapter 1 – History and Motivation	5
1.1 History of Thin Metal Films Deposition	5
1.2 Motivation	7
Chapter 2 – Vacuum Deposition and Thin Film Background	8
2.1 Vacuum Technology	8
2.1.1 Vacuum Chambers	8
2.1.2 Vacuum Pumps	9
2.1.3 Vacuum Pressure Measurement.....	13
2.2 Evaporation Devices	15
2.3 Film Formation and Monitoring	19
2.3.1 Film Growth	19
2.3.2 Deposition Monitoring	20
2.3.3 Film Microstructures and Properties.....	23
Chapter 3 – Theory	27
3.1 Mean Free Path and Knudsen Number	27
3.2 Evaporation Theory	30
3.3 Thickness Distribution	36
Chapter 4 – Description of Apparatus	38
4.1 Overview	38
4.2 Top and Bottom	40
4.3 Substrate Mounting Plate	42
4.4 Body	44
Chapter 5 – Results and Conclusions	48
5.1 Initial Results	48
5.2 Future Work	50

TABLE OF FIGURES

Figure 1. Early Thomas Edison deposition chamber	6
Figure 2. O-ring and conflat flange seals.....	9
Figure 3. Modern oil-sealed rotary vane pump diagram.....	10
Figure 4. Cycle of an oil-sealed rotary vane pump	10
Figure 5. General turbomolecular pump diagram	12
Figure 6. Adsorption of atoms to turbomolecular blades.....	12
Figure 7. Dunlap and Trump thermocouple gauge.....	14
Figure 8. Bayard-Alpert ionization gauge.....	14
Figure 9. Simple sputtering device.....	15
Figure 10. Filament versus crucible evaporation	16
Figure 11. Apparatus for both filament and crucible evaporation	16
Figure 12. Electron beam evaporation device.....	17
Figure 13. O'Bryan e-beam heated crucible device	18
Figure 14. Four stages of film growth.....	20
Figure 15. Ion evaporation rate monitor.....	22
Figure 16. Miller index examples	23
Figure 17. Electron backscattered diffraction maps of thin silver films	24
Figure 18. Ion beam assisted deposition chamber	25
Figure 19. Closest approach and classical collision cross section.....	27
Figure 20. Atomic relative velocities	28
Figure 21. Solid or liquid and its vapor in a sealed container.....	32
Figure 22. Evaporation from a hemispherical source.....	33
Figure 23. Predictions for the deposition rate of silver	35
Figure 24. Thickness distribution diagram.....	37
Figure 25. Overview diagram of the Houghton College deposition chamber.....	38
Figure 26. Diagram of the Houghton College evaporation hardware	40
Figure 27. Scale drawing of the top of the chamber	41
Figure 28. Scale drawing of the bottom of the chamber.....	42
Figure 29. Scale drawings of top and side of substrate mounting plate	43
Figure 30. Scale drawing top view of body	45
Figure 31. Scale drawing side view of body	46
Figure 32. Specifications for feedthrough positions	47
Figure 33. Installed feedthroughs at the bottom of the deposition chamber.	48
Figure 34. Front and back view pictures of deposition chamber.....	49

HISTORY AND MOTIVATION

1.1 History of Thin Metal Films Deposition

Thin metal films have been produced for over a hundred years with one of the first cases of metallic deposition being noted by W. R. Grove in 1852 [1]. Grove was researching the conducting properties of various gases by viewing the effects of arcing between electrodes in different atmospheres. In doing so, small amounts of metal were deposited from the electrodes and were visible on the apparatus. This provides one of the first examples of physical sputtering of metals.

Five years later, Michael Faraday similarly evaporated various metals by electrical discharge, studying the optical properties of the deposits produced [2]. In this experiment however, he was intentionally using the deposition process discovered by Grove and perhaps others, to examine the interactions of light with gold and other metals. Faraday deposited gold, tin, lead, and other metals onto glass substrates, and noted how each reflected and transmitted polarized light.

Similarly, in 1877 Arthur W. Wright researched the production of various metallic films on the inside of a vacuum tube, evacuated by a mercury pump [3]. This provides one of the earliest cases of physical vapor deposition at a pressure less than atmospheric. Wright, like Faraday, also used various metals and sputtered them using an electric discharge.

Generally speaking, it was in experiments such as these mentioned that the deposition of thin films was first noted and utilized. While the process was discovered accidentally, by the end of the 19th century the importance of the produced films was becoming apparent in areas beyond research. Thomas Edison had realized their practical use, filing several U.S. Patents on the production of phonographs utilizing the deposition of metals under vacuum [4][5][6][7].

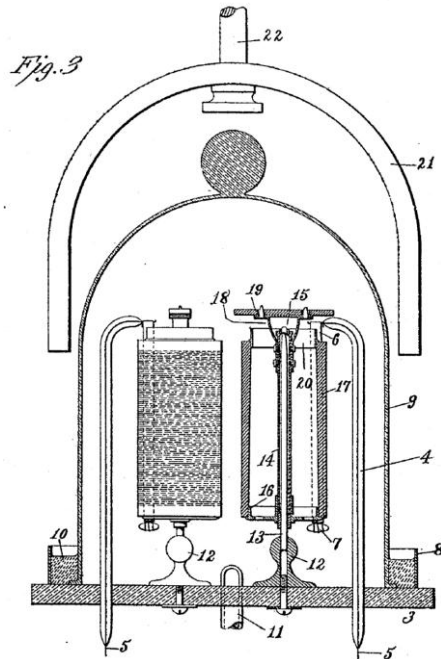


Figure 1. An Edison deposition chamber, patented in 1904 showing the bell jar chamber (9) and various devices specifically for phonograph production. Wires (5) lead to electrodes producing metal evaporate upon electrical discharge (6). Figure taken from Ref. [7].

Up to this point, sputtering from an electrode was the dominant form of deposition, but this would change with the advent of other processes. Many of their key features are still utilized today and are discussed in Section 2.2. The history of the production of thin metal films however, hinges directly on advancements in vacuum technology. Evaporating metals under vacuum has a couple advantages. First, evaporated atoms will not diffuse as they travel through the vacuum and second, the likelihood for contamination of the film decreases drastically. Therefore, a vacuum is the obvious choice for the production of thin films.

Early pumps removed air mechanically. In 1905, Walter Gaede invented the rotary mercury pump allowing much lower pressures to be attained than were previously possible with pistons or other mechanical means [8]. Gaede became central to the advancement of vacuum technology by going on to invent the mechanical forepump, the molecular pump in 1913, and the diffusion pump in 1915. Advancements in both mechanical pumps and diffusion pumps continued into the early 1900's, followed by the ion pump in 1958 and the cryopump soon afterwards [8]. Through these advancements, the lowest attainable pressure went from a few torr at the beginning of the century, to

less than 10^{-10} torr by 1950. Accordingly, the ability to produce thin metal films of higher purity and for metals that are more difficult to evaporate followed.

1.2 Motivation

Since the early studies of thin films and advances in technology, thin films have become widely used in a variety of industries. They are found in applications ranging from reflective coatings for mirrors to conductive material for microprocessors, but much remains to be discovered about the atomic-scale processes that determine their microstructures and the resulting properties as compared to their bulk materials.

A vacuum deposition chamber is currently being constructed at Houghton College to explore these processes further. Upon completion, the capacity to fabricate thin metal films will be attained, presenting the opportunity to research the affect that various deposition conditions have on the produced film.

One specific area that will be explored is how the thickness of thin metal films changes their preferred grain orientation and how this affects the stress and strain of the film. This has been studied by students at Houghton College in the past and will be a continued priority in the future. To this end, a computer-controlled shield will be added to the deposition chamber to allow for the deposition of films with a thickness gradient, thereby decreasing the number of samples that need to be produced to study this thickness-dependent phenomenon.

Secondly, an ion gun will be included to clean the substrates before depositing and to increase the available energy at the surface of the substrate during deposition. This process is called ion-beam assisted deposition (IBAD). By adding additional energy to the substrate, adatoms are given more mobility to move and create a more uniform and continuous film with different microstructural properties.

VACUUM DEPOSITION AND THIN FILM BACKGROUND

2.1 Vacuum Technology

2.1.1 Vacuum Chambers

The ultimate design of different vacuum chambers depends on their intended use, specific to each case. For thin films, there are different considerations such as the distance from the source to the substrate, the necessary feedthroughs to produce films, and how to make all of the systems work together. For example, one aspect specific to thin films production is that metal atoms typically evaporate in many directions and form a film on the walls and other areas of the chamber. As a result, precautions need to be taken to block pump inlets and other features that may be sensitive to the evaporated flux.

For vacuum chambers, it is necessary to carefully select the components in contact with the evacuated region. These choices are limited to materials that have low vapor pressures and high outgassing rates. The former is the partial pressure of the material and the latter depends on its ability to adsorb or absorb different elements and molecules. In vacuum environments, it is necessary to keep the vapor pressure of all components well below the pressure of the system because, as the two approach one another, the evaporation rate of the material increases causing a higher residual pressure. Similarly, materials that have low outgassing rates slowly emit trapped molecules over a long period of time, which is detrimental to high vacuum systems. In many cases, low vapor pressure materials specifically designed for vacuum use can be purchased.

There are different ways to decrease outgassing effects. The first is to remove the adsorbed molecules. According to a study completed by the American Vacuum Society (AVS) the following steps are the most commonly followed for cleaning a variety of materials [9]. For material-specific treatments, see Ref. [9]. First, after physically removing as many contaminants as possible, vapor degreasing is used to remove loosely bound, heavy molecules. This is then followed by chemical cleaning steps such as alkaline cleaning, acid etching, electro-polishing, or a combination of the three. Lastly, the components

are rinsed with deionized or distilled water. Aluminum specifically, forms a porous oxide which acts as a possible trap for molecules and limits the outgassing rate [9]. This layer has been minimized by cleaning with a solution of Almecco 18 at 65°C [10].

The second strategy for minimizing outgassing effects is to initially increase the outgassing rate through baking. Baking involves heating a vacuum chamber to remove adsorbed residual gases faster, while the system is being pumped. After all components are cooled, the pressure of the system is lower than an unbaked chamber having been evacuated for the same period of time. For aluminum systems, it is recommended that baking is completed at 150°C for a duration of at least 24 hours [11].

Just as important as which materials to select for a vacuum chamber and how to clean and bake them is how the components are to seal together. Viton o-rings and gaskets or metal gaskets are often utilized for this purpose [12]. For the attainment of high vacua, it is common to use metal because it adsorbs fewer molecules than Viton and does not allow permeation of water [13]. In addition, metal gaskets are able to withstand high temperatures for baking while Viton is limited to 120-200°C [11]. An advantage to Viton, however, is that it is reusable and can be more cost effective for some applications. These gaskets and o-rings also do not require stainless steel conflat flanges as do metal gaskets. An o-ring channel and a conflat flange are depicted in Figure 2 with the o-ring and gasket shown in black. In both cases, they are commonly compressed using bolts or screws.

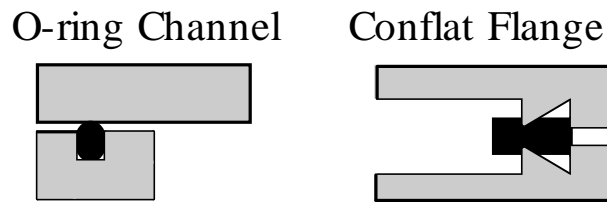


Figure 2. Common joints to seal vacuum components. O-rings can be used with both whereas metal gaskets are only used with conflat flanges. Bolts or screws are typically used to compress the seal. The seal is represented in black.

2.1.2 Vacuum Pumps

To evacuate a sealed chamber, a vacuum pump must be used. The original oil-sealed rotary pump was invented by Walter Gaede in the early 1900s and the general concept is still in use [14]. A simple example of an oil-sealed rotary vane pump is illustrated in Figure 3.

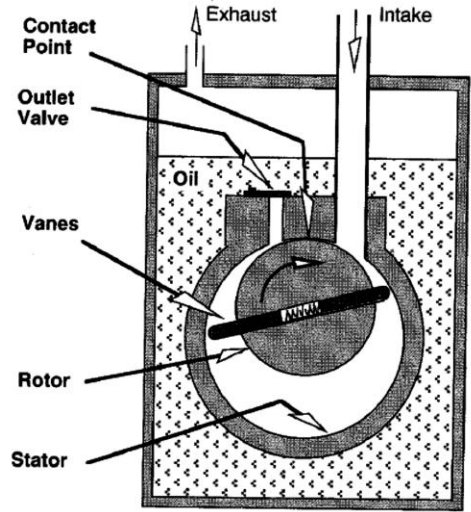


Figure 3. Diagram of a modern oil-sealed rotary vane pump with major components labeled. Axis of rotor is offset from that of the stator with contact point and ends of vanes sealed to the stator by a thin layer of oil. Figure taken from Ref. [15].

The intake side of the pump is connected to the chamber to be evacuated and, as the rotor is turned by a motor, gas enters the intake and is forced out the outlet valve and, eventually, the exhaust. The process is shown in Figure 4.

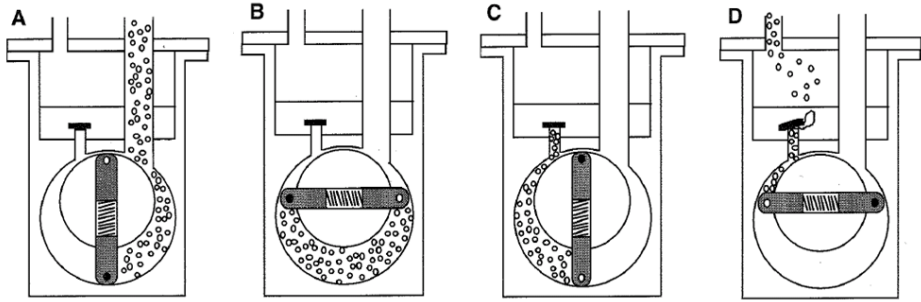


Figure 4. Complete cycle of an oil-sealed rotary vane pump showing intake atoms and molecules pulled into the pump (A), closing them off to the intake (B), and finally forcing them out the exhaust and out of the pump (C and D). Figure adapted from Ref. [15].

The oil is very significant to the operation of rotary pumps. It not only acts as a lubricant, but also a coolant and a sealer. As the outlet valve opens, a small amount of oil leaks between the stator and rotor, cooling the inside and sealing the vanes and contact point with a thin layer of oil.

The rotary pump is often used as a roughing pump to achieve a sufficiently low pressure for the operation of high vacuum pumps and also as a forepump to provide a lower pressure at the outlet of these devices. It works best when the gas is characterized by fluid flow (low Knudsen number, see Section 3.1) and as such, is limited in the vacua that it can achieve. To obtain lower final pressures, it is common to place two rotary pumps in series, “two-stage”, with the outlet of the first connecting to the inlet of the second. This allows for even lower pressures that are commonly at 10^{-3} torr [15].

To obtain lower pressures than this, it is common to use different styles of pumps. The turbomolecular pump is designed to operate in systems where the motion of the residual gas particles is defined as molecular flow (high Knudsen number, see Section 3.1). It therefore is commonly used to produce the final pressures in high vacuum systems after the chamber has been evacuated using a roughing pump. These pumps can produce pressures as low as 10^{-9} torr [12]. The following discussion regarding this pump is taken from Ref. [15].

The turbomolecular pump uses blades attached to a rotor spinning at speeds of up to 90,000 RPM to give molecules a preferred direction, through the pump and out of the vacuum system. A cross section view of a turbo molecular pump is shown in Figure 5a). Figure 5b) shows how the rotating and stationary blades direct molecules out of the system, however, it is slightly misleading. In fact, molecules colliding with the blades of the rotor and stator do not strike and leave the surface instantaneously but adsorb for a period of time. This is illustrated in Figure 6.

Figure 6 explains why the blades travel at such high velocities. If the blade velocity is comparable to that of the average molecular velocity, it becomes much less likely for molecules to approach from behind and adsorb to the back of the blade. Therefore, if the majority adsorb to the front, they are also most likely to desorb towards the outlet of the pump. This is how a turbomolecular pump removes molecules from the vacuum chamber.

Notice that for thin film applications using turbomolecular pumps, it is essential that the system protect the spinning blades from any deposition source or other object that could damage the blades or affect their precise balance. It is common to use shields placed in front of the inlet of the pump for this purpose.

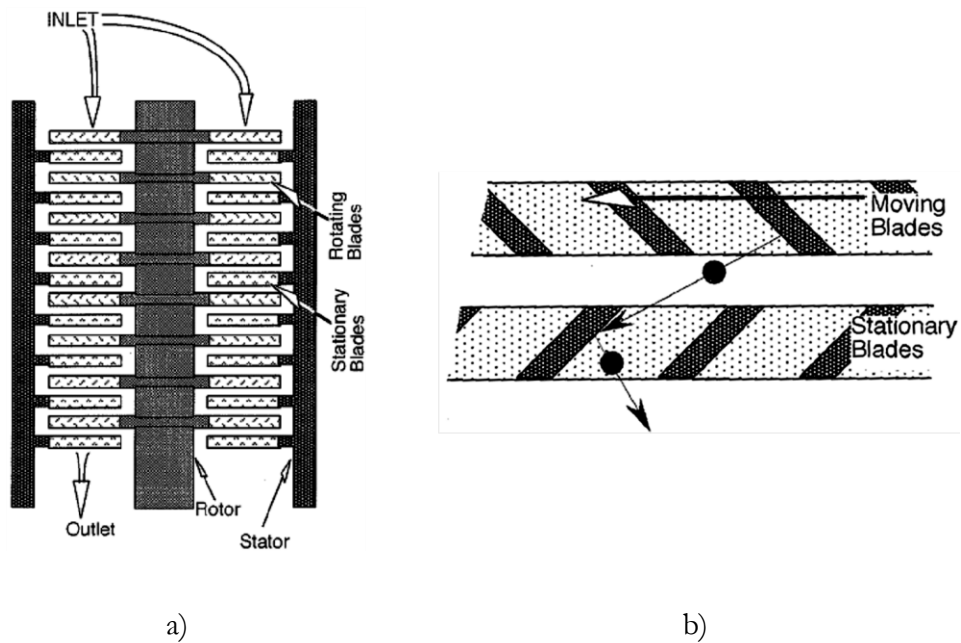


Figure 5. General turbomolecular pump apparatus. a) Internal components of pump. Rotor spins relative to stator causing the moving blades and stationary blades to give molecules a preferred direction, forcing them out of the pump. b) Close view of moving blades and stationary blades forcing a molecule out of the vacuum. Figures taken from Ref. [15].

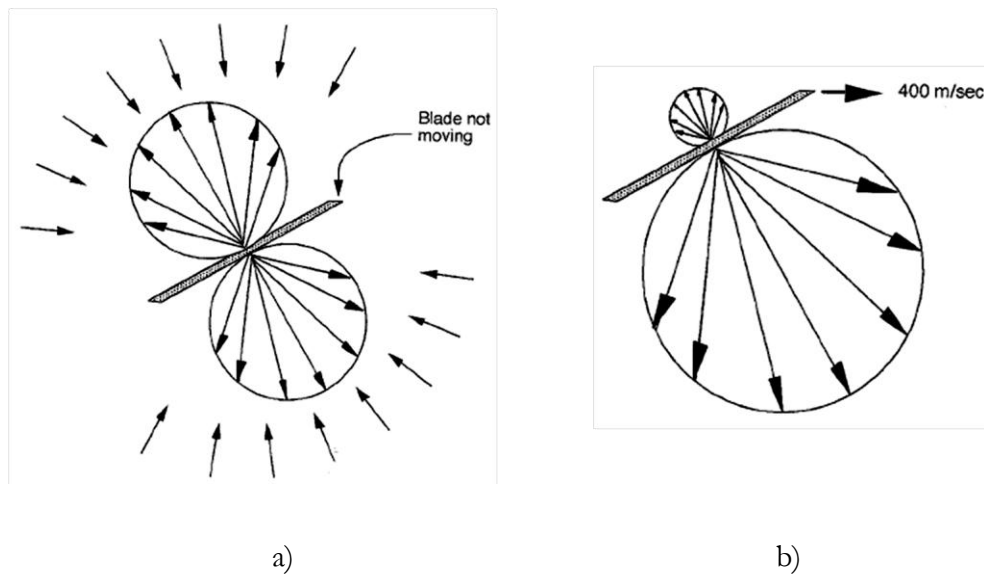


Figure 6. a) Arrows indicate first adsorption of molecules to the surface of the blade (towards the blade) followed by desorption (away from the blade) in a cosine distribution. b) If it is moving close to average molecular velocity, adsorption and desorption become more probable on front as illustrated by the larger arrows. Figure taken from Ref. [15].

2.1.3 Vacuum Pressure Measurement

After a system has been evacuated, it is necessary to determine the pressure. Two common instruments utilized are the thermocouple and ionization gauges. In many deposition chambers, the thermocouple gauge is used during rough pumping, followed by an ion gauge after high vacuum has been attained and the thermocouple gauge has measured under-scale.

Thermocouple gauges operate as follows [16]. Energy is dissipated from a hot surface by both radiation and conduction. At low pressures, where the mean free path is longer than the distance between hot and cold surfaces, the energy loss by conduction is strongly dependent on the gas pressure between the surfaces. Therefore, by supplying a constant energy to a filament, the temperature of the filament will change depending on the pressure of the system. By measuring the temperature with a thermocouple, the correlation can be calibrated to measure the pressure in proximity to the gauge. Thermocouples are generally good for measurements between 1 torr and 10^{-3} torr.

An early example of a thermocouple gauge is the device proposed by G. C. Dunlap and J. G. Trump [17]. Their apparatus is shown in Figure 7. As the thermocouple wires are heated, a potential difference proportional to the temperature is produced and is measured using an ammeter of known resistance.

Because thermocouple gauges are limited to pressures above 10^{-3} torr, ion gauges are typically used in high vacuum systems. Their operation uses accelerated electrons to ionize residual gases [18]. These ions are then collected and the resulting current is measured. Because this current is proportional to the number of ionized particles and there is a given probability for ionization, it is also proportional to the pressure.

After many design changes to the earliest ion gauges, the lowest measurable pressure was extended from 10^{-8} to 10^{-10} torr, resulting from the work of Bayard and Alpert [19]. Their apparatus utilized a wire for the ion collector. Because this minimized the surface area, it decreased the likelihood that x-rays could cause the photoelectric emission of electrons, resulting in a background current. This advancement is still commonly used in ion gauges.

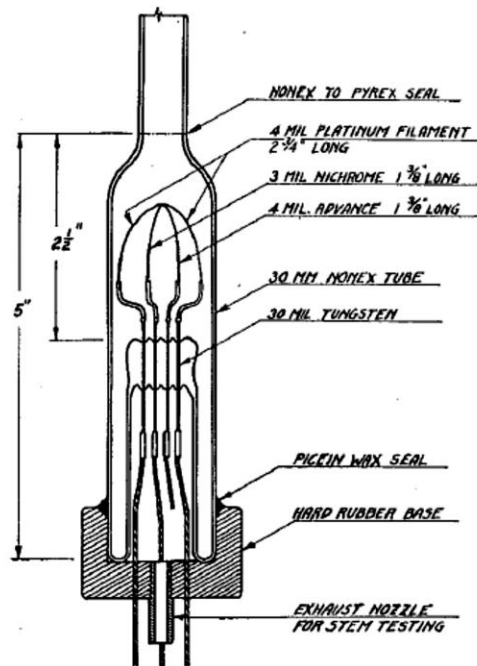


Figure 7. Dunlap and Trump thermocouple gauge. The platinum filament and thermocouple are visible. The thermocouple is made of a 3 mm nichrome wire and a 4 mm advance wire. Figure taken from Ref. [17].

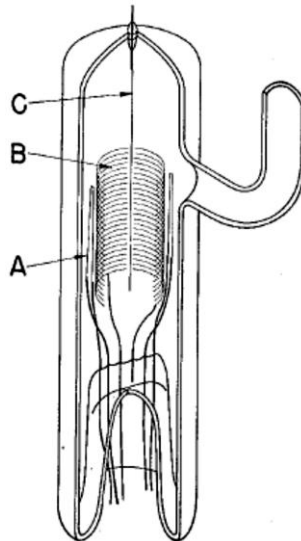


Figure 8. The Bayard-Alpert ionization gauge. The cathode (A) is heated causing thermionic emission of electrons that are accelerated towards the positive potential at grid (B). Collisions with residual gases create ions that are attracted to the negative biased collector (C). Figure taken from Ref. [19].

2.2 Evaporation Devices

There are a variety of ways to deposit thin films, but vacuum deposition has become one of the most widely used. Two common types of deposition under vacuum are sputter deposition, in which the source is bombarded with energetic ions, and thermal deposition where the source material is heated to vaporization.

Sputter deposition, or “sputtering”, is different from thermal deposition because the source is not heated to vaporization but is bombarded with ions, breaking off small groups of atoms [20]. This is depicted in Figure 9. Sputtering is advantageous because it does not require vaporization of the source, enabling the deposition of metals that vaporize at high temperatures. In addition, if more contamination can be tolerated, sputtering does not require as low a vacuum as thermal deposition. Collisions with residual gases between the source and substrate have less of an effect on the direction of the clusters of atoms as opposed to individual atoms from vaporization.

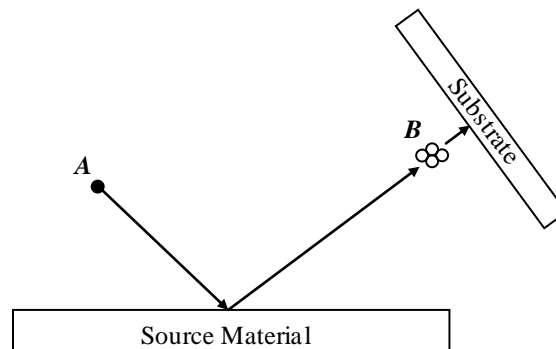


Figure 9. Simple sputtering device showing an energetic ions (*A*) bombarding the source material and imparting momentum to a small piece of the source (*B*) that travels to and is adsorbed onto the substrate.

Thermal deposition, unlike sputtering, involves heating the source until evaporation and placing a substrate in the path of the evaporated flux. These systems have the advantage of being easier to construct than some sputtering devices. Examples of thermal techniques include resistance and electron beam heating.

Resistance heating is a broad category of thermal deposition that utilizes the heat produced by electric current in a wire [21]. In some cases, the source metal is melted directly onto a filament for

evaporation (Figure 10a) [22]. One downside with this particular strategy is that the evaporated flux travels in nearly all directions. While this can be circumvented by using shields, using a crucible (Figure 10b) limits the directionality and enables the evaporation of metals with low vapor pressures. Metals like this will sometimes melt before achieving a high evaporation rate and could drip from the filament. A crucible however, can contain molten materials and increase the likelihood that they can be deposited.

A novel system that is able to evaporate directly from a filament or from a crucible is depicted in Figure 11. In this case, the resistive wire has been shaped so it can support a crucible when not being used for direct filament evaporation.

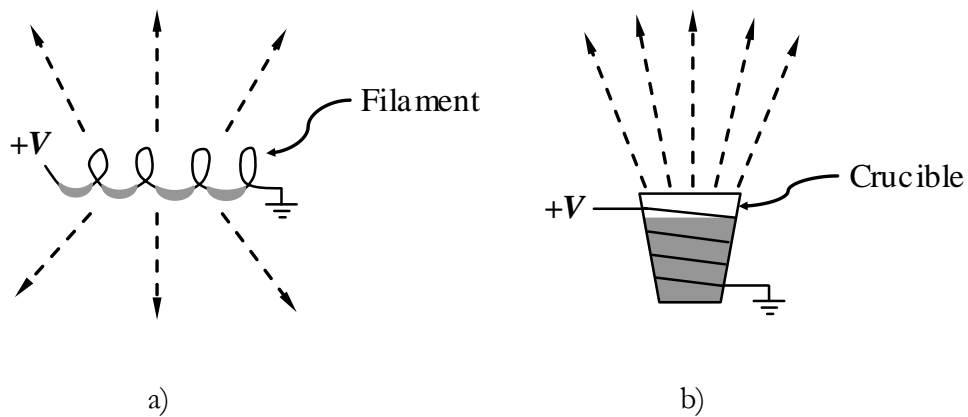


Figure 10. a) Metal evaporated directly from a resistively heated filament, spreading in all directions. b) Evaporation from a resistively heated crucible, spreading much less.

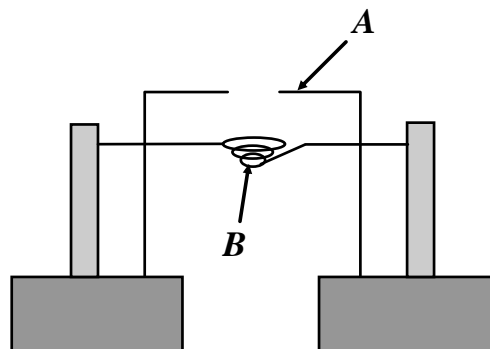


Figure 11. Deposition source able to deposit directly from filament or from crucible placed inside filament, **B**. Notice shield, **A** to limit directionality of flux when evaporated from filament. Figure adapted from Ref. [23].

Additional constraints to direct filament evaporation are how different metals wet, react with, and evaporate from various filament materials [24]. The use of crucibles to hold material is common with thermal deposition techniques because there is less dependence on these characteristics.

In addition to resistive heating, a second common form of thermal deposition is electron beam (e-beam) evaporation. In this technique, an electron beam is incident on the source causing localized heating and the crucible is commonly cooled. As a result, e-beam evaporation has advantages over resistive heating such as higher deposition rates and a decrease in the contamination of the produced film. The attainable deposition rate is increased because more power can be delivered through an e-beam than through a wire, which is limited by high currents. Also, by keeping the crucible cool, the likelihood of temperature-induced interactions with the source metal decreases. This cannot be accomplished when using a crucible with resistance techniques because the source is heated through it.

An example of an e-beam system is depicted in Figure 12. A common variation on this places the gun underneath the source, utilizing a magnetic field to bend the beam to the surface of the metal, potentially decreasing the likelihood of sputter contamination. This contamination is a disadvantage to e-beam deposition that results from positive ions, created during deposition, being inadvertently accelerated towards the negative accelerating grid in the gun, causing the gun material to be sputtered. Another downside to e-beam evaporation is that, in many cases, a large amount of power is required for effective evaporation. While this is dependent on the material, some metals require approximately 6 kW of power to yield an appreciable evaporation rate [25]. Additionally, magnetically focused and directed e-beam sources are difficult to construct and can prove challenging to focus properly.

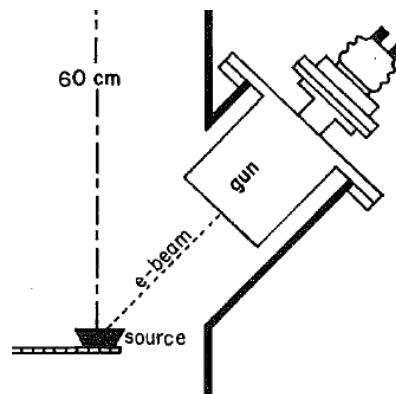


Figure 12. Electron beam deposition system showing e-beam directly incident on source material. Figure taken from Ref. [26].

H. M. O'Bryan created an apparatus for vacuum deposition that combined both thermal and e-beam techniques while eliminating some of the downfalls of each [27]. O'Bryan evaporated metals by bombarding the surface of a graphite crucible with electrons, accelerated through a potential difference between a tungsten filament and the crucible itself. Therefore, the source is heated by the accelerated electrons via the thermally conducting crucible, as well as resistively as the electrons travel through the crucible, completing the circuit. While limited by the melting temperature of the graphite at about 3500°C, he found success in evaporating many metals with melting points up to 2600°C.

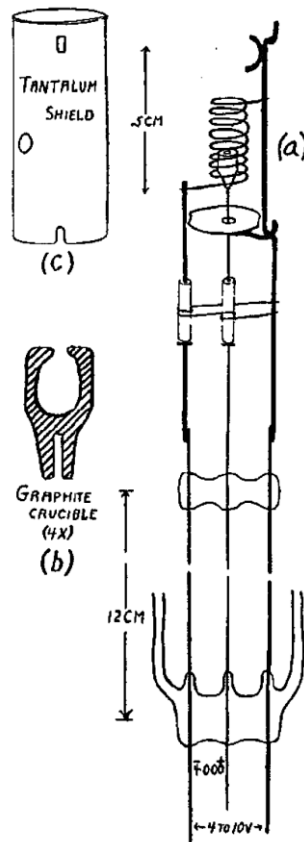


Figure 13. O'Bryan's apparatus featuring an e-beam heated graphite crucible (a). To further limit deposition directionality, a tantalum shield (c) is placed around the filament. Figure taken from Ref. [27].

A downside to O'Bryan's apparatus is that care must be taken to make sure that there are no reactions between the crucible and the metal. This is more of a problem with this apparatus than with a typical e-beam source because the crucible and metal are heated together like in resistive heating. Another disadvantage is the opportunity for sputter contamination as mentioned for e-beam techniques.

This approach does, however, have the following advantages over e-beam and resistive heating. First, it has a power advantage over each. At a maximum, O'Bryan's apparatus supplied 500 W at an accelerating potential of 5 kV and was able to evaporate molybdenum at 2600°C. Using a typical e-beam gun, E. B. Graper reports a power of 4 kW required for a stable deposition rate for the same material [25]. Also, an apparatus such as O'Bryan's is easier to construct than an e-beam source that needs to be accurately focused onto the surface of the metal. The power advantage over resistive heating is that this apparatus is not limited in the high current that can be supplied.

2.3 Film Formation and Monitoring

2.3.1 Film Growth

After metals have been vaporized and the evaporant has travelled through the vacuum region between the source and the substrate, it strikes a substrate and begins to form a thin film. Adsorption is the “sticking” of atoms and molecules to a surface both physically and chemically and therefore controls the process by which films are formed. While the physics of adsorption is quite complex, there are two parameters which play a significant role. As discussed by I. Langmuir both a decrease in substrate temperature and an increase in incident flux will cause the number of adsorbed atoms to go up [28].

Adsorption is temperature dependent because, according to Langmuir's theory, atoms are adsorbed in almost all cases, with the temperature affecting how long the atoms remain in contact with the surface. Langmuir theorized further that the higher the incident flux, the more energy is required to evaporate the adsorbed atoms due to internal interactions between them. This combination is often noticed in the early stages of growth as atoms form small clusters called nuclei.

The process of deposition generally involves four distinct steps: nucleation, growth and combining of nuclei, the formation of channels, and the formation of a continuous film with holes being filled [29]. These are illustrated in Figure 14. The following description of the four stages is based on direct observations from Ref. [29]. In this experiment, gold and silver were deposited onto a thin molybdenum disulphide substrate in the column of a transmission electron microscope, allowing deposition and sub-micron viewing simultaneously. The apparatus also allowed for continuous viewing of the substrate whether the incident flux was blocked or not. This allowed for time evolution studies of films, post-deposition. The microstructure of growing films is discussed in Section 2.3.3.

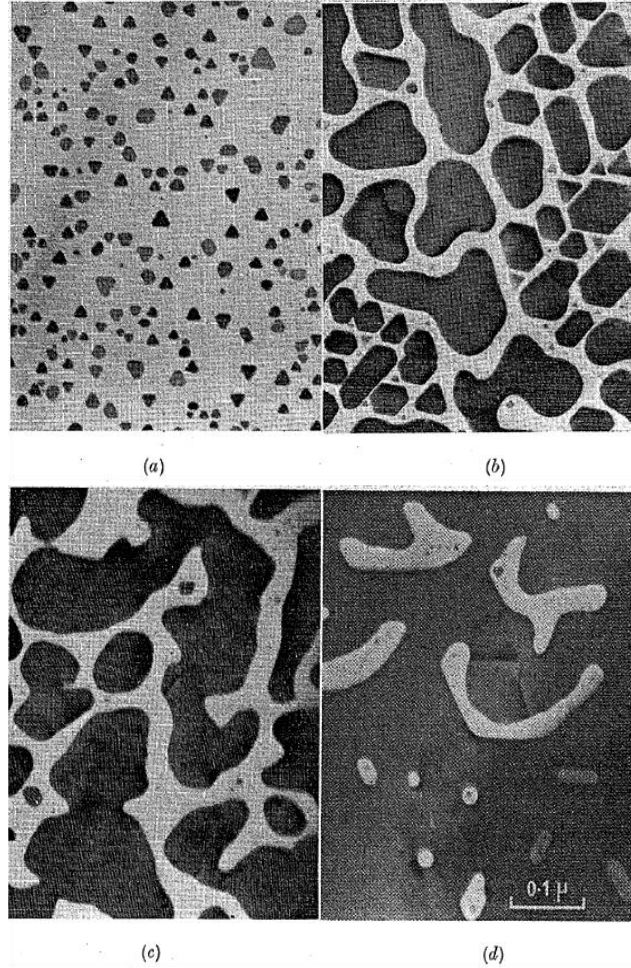


Figure 14. Micrographs showing the four different stages of film growth of gold deposited on MoS₂ at 400°C. Films were deposited in a transmission electron microscope and magnified x 130,000. Stages are: a) nucleation, b) growth and coalescence of nuclei, c) formation of channels, and d) continuous film, filling in holes. Figure taken from Ref. [29].

2.3.2 Deposition Monitoring

To produce a film of specific thickness, it is necessary to at least find an approximation for the rate, or the thickness of the film during the deposition process. One of the most commonly used methods for measuring thickness is through the measurement of the resonance frequency of a thin quartz crystal [30]. The resonance frequency of a quartz crystal depends on its thickness d and the speed at which the waves propagate through the crystal, v . This relationship is given by

$$f = \frac{v}{2d}. \quad (1)$$

Therefore, by depositing metal onto the crystal and measuring the change in frequency, the thickness of the deposited film can be calculated. Notice that the location of the crystal relative to the substrate will affect this measurement due to the reasons presented in Section 3.3.

Other methods for thickness monitoring involve the time integration of the rate of deposition. For these methods, the rate of deposition can be determined through measurable quantities that are proportional to the rate of film growth. Examples include the measurement of the temperature of the metal and measurement of ionized vapor using an ion gauge in the path of the evaporant. These methods commonly use a shield to block the metal vapor from the substrate until a constant rate of deposition has been achieved. If the thickness is given by D and the time as t

$$D = \int_0^T \frac{dD}{dt} dt = T \frac{dD}{dt}. \quad (2)$$

Notice in Equation (2) that the total time of deposition is given by T . Therefore, as long as a suitable way to determine this rate is found, it can be used to determine the thickness.

Temperature monitoring as a means to measure the deposition rate relies on the predictions of the Hertz-Knudsen equation, Equation (22). While the temperature dependency is not clear because the vapor pressure is also a function of the temperature, individual predictions can be used initially if the vapor pressure at given temperatures is known. A more accurate, empirically determined calibration can be found by first allowing thermal equilibrium to be reached before starting deposition. Next, by noting different deposition times and the film thicknesses yielded, the rate as a function of temperature can be plotted and used for thickness rate monitoring.

Advantages to this method are that it does not rely on the geometry of the chamber like a crystal monitor and only a thermocouple is required for monitoring. There are disadvantages, however. First, the deposition rate is not measured directly, but is calculated from the temperature of the crucible. Also, calibrations will need to be determined separately for different source metals because the evaporation rate is dependent on the properties of the material, as predicted in Equation (22). If a

separate calibration is found for each however, temperature monitoring may be a viable means to predict film thickness during deposition.

A second technique for monitoring the deposition rate utilizes ion gauge technology [31]. By positioning an ion gauge apparatus in the path of the evaporated atoms, a fraction of the atoms will be ionized and can be collected. Because the number of atoms ionized is dependent on the number available, the rate of deposition will be proportional to the measured current from the collected ions.

The device proposed by Giedd and Perkins is depicted in Figure 15. A filament is placed inside the anode which it is held at +155V with respect to ground. The electrons are accelerated through this gap and collide with atoms of the evaporated flux, causing a percentage of them to be ionized. Some will pass through the cylindrical anode and are accelerated towards the collector held at -20V relative to ground. This collector current is measured and a calibration for the deposition rate is found empirically.

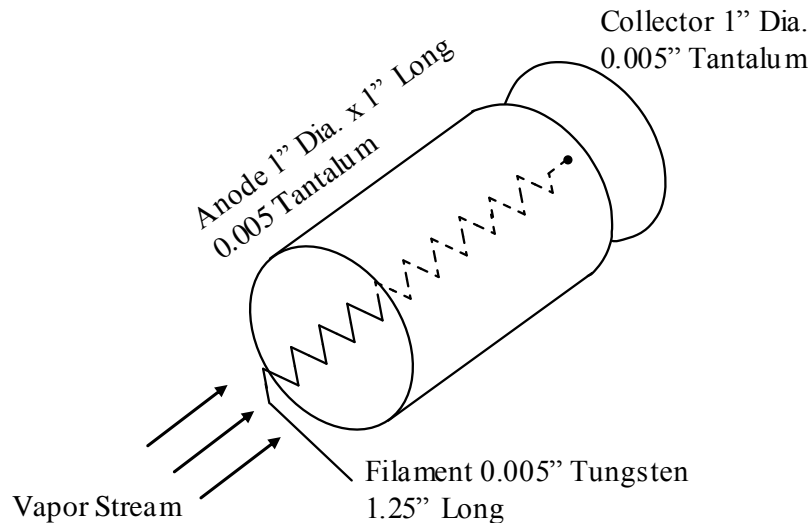


Figure 15. Ion evaporation rate monitor using thermionic electron emission from a tungsten filament to ionize metal vapor. Anode potential is +155V and collector potential is -20V relative to ground. Ions are accelerated towards the collector and a current is measured. Figure adapted from Ref. [31].

While this method is susceptible to geometry effects on thickness and calibrations will be affected by different source metals, it does not have some of the problems associated with crystal monitors or temperature monitoring. First, ion gauge monitors can be built at a fraction of the cost of crystal

monitors and they make direct measurements of the flux unlike temperature techniques. Also, if residual gases are found to produce a large background current, an identical monitor can be placed outside of the vapor path to measure it specifically. This can then be subtracted from the current monitored by the first gauge, yielding a more precise measurement depending on the ionized flux only.

2.3.3 Film Microstructures and Properties

Current thin metal films research primarily relies on microstructure studies. The properties of the films are dependent on their atomic features, characterized by the orientation of the atoms relative to the substrate. In research, it is common to use Miller indices, $\{hkl\}$, to define this orientation [32]. Consider a grid like those depicted in Figure 16. The Miller indices are defined as the inverse of the smallest x , y , and z intercepts for lines drawn through the points, forming planes. Lines that pass through the origin are ignored because they have an intercept of zero.

As an example, in Figure 16a), the smallest x and y intercepts are noted in the bottom leftmost line, each with a value of one. Therefore, this is represented by (11∞) . Infinity represents a line intersecting at an infinite distance which is the case for the z intercept here. Because the Miller index is the inverse of this minimum intercept, for the planes in a) it is $\{110\}$ for $\{hkl\}$. Other examples are given in Figure 16. Notice that negative numbers are represented by a dash above the number. For example, -1 is represented as $\bar{1}$. This is shown in Figure 16b) with the planes having a $\{\bar{1}10\}$ orientation.

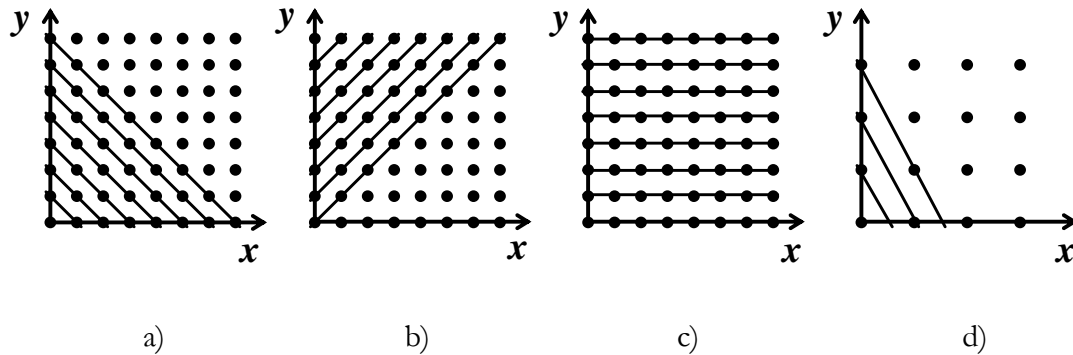


Figure 16. Two dimensional examples using Miller indices. The x and y axes are labeled and the points represent the periodic arrangement of a given crystallographic feature. Notice that each plane intersects the z -axis at infinity. a) $\{110\}$ b) $\{\bar{1}10\}$ c) $\{010\}$ d) $\{210\}$.

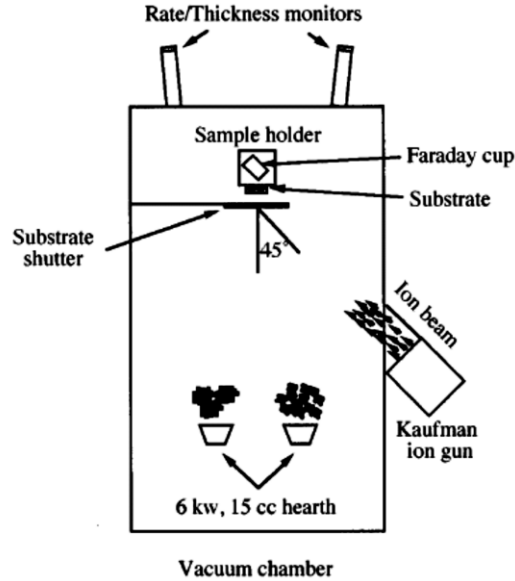


Figure 18. Vacuum chamber for studies of IBAD on microstructure properties of metal films. Faraday cup measures current from ion gun. Figure taken from Ref. [37].

Ion assisted techniques in general have been shown to increase the density, inhibit surface roughness, and control, to some extent, the density and orientation of thin films [34]. Important to the effects of IBAD on microstructural properties are both the energy of and the arrival rate (relative to metal vapor) of the ions. For example, it has been found that increasing the ion energy and/or arrival rate ratio increases the surface roughness in thin niobium films [37]. Similar studies can be completed for other metals and can be extended to grain orientations and defects also.

In addition to IBAD, the thickness of films has been shown to affect their preferred grain orientation [38]. This is a result of competing energy minimization processes that dominate the growth and formation of the microstructure [34][39]. Throughout film formation, the minimum total energy is sought from a combination of the surface, interface, grain boundary, and structural energies. Surface energy depends on the structure of the upper surface of the film, the interface energy from the epitaxial effects between the metal and substrate, the grain boundary energy from interactions between different grains, and structural energy from properties internal to individual grains. As a result, surface and interface energies remain relatively constant throughout film growth, however, grain boundary and structural energies increase with thickness. The former two energies dominate early microstructure formation but, as deposition continues, they are overtaken by the drive to minimize the latter two.

In silver films specifically, as the thickness increases, the preferred grain orientation changes from $\{111\}$ to $\{100\}$ over a range from 0 to 1500 nm in thickness [38]. This is shown in the Electron Backscattered Diffraction maps in Figure 17. Notice that in the 1500 nm film, the $\{100\}$ orientation dominates and is also many times the size of the original $\{111\}$ grains that characterized the 100 nm film.

THEORY

3.1 Mean Free Path and Knudsen Number

Lowering the residual pressure of the system reduces the number of collisions between source atoms and residual gas molecules. This decreases the diffusion of the evaporated flux and also the likelihood for contamination of the evaporant and substrate. A relationship for the mean free path, the average distance between collisions, can be derived as follows [40]. To be corrected later, the initial assumptions are that only the target particle is moving and that there is only one possible collision particle. The average distance, L , that an atom travels in time dt is given by Equation (3), where \bar{v} is the average velocity of the target atom

$$L = \bar{v} dt . \quad (3)$$

The volume, within which a collision is possible, is given by the length traveled from Equation (3), multiplied by the collision cross section. By assuming that all atoms in the system are of equal size and are spheres of diameter d , this quantity can be determined. This formulation of the cross section ignores the effects of quantum mechanics, but an order-of-magnitude estimate is obtained.

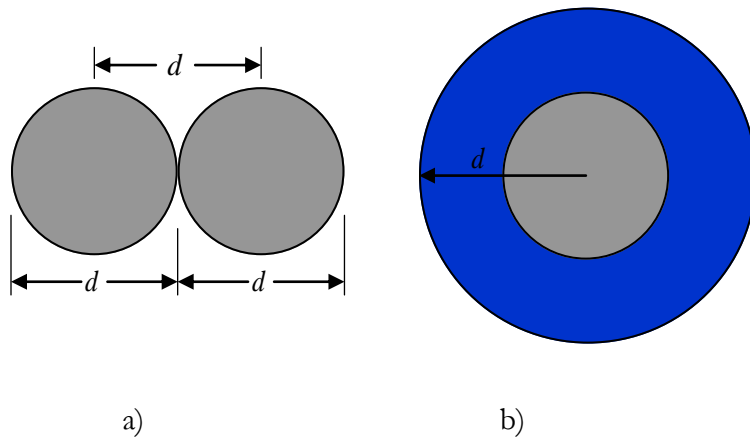


Figure 19. a) Closest approach between two atoms of the same diameter. b) The collision cross section has a radius equal to the diameter of the atoms.

As seen in Figure 19, for a system containing particles of equal diameter d , the collision cross section has a radius d and is therefore given by

$$\sigma = \pi d^2 . \quad (4)$$

Multiplying Equation (3) and Equation (4) yields the volume containing the collision

$$\sigma \bar{v} dt = \pi d^2 \bar{v} dt . \quad (5)$$

At this point, the corrections are made for the velocities of all particles in the system and the system is expanded to more than one collision particle. If all particles have an average velocity \bar{v} , notice that \bar{v} in Equation (5) is actually a relative velocity between the target and collision particles. Also, it is more general to include N/V collision particles, where N is the number of molecules in a region of volume V . With both of these corrections, Equation (5) becomes

$$\frac{N}{V} \pi d^2 v_{rel} dt . \quad (6)$$

Notice that this represents the number of collisions that a molecule has in time dt , or in other words, is the frequency of collisions. Next, a relationship for v_{rel} in terms of the average velocity \bar{v} can be found by considering multiple particles with different velocity vectors as depicted in Figure 20.

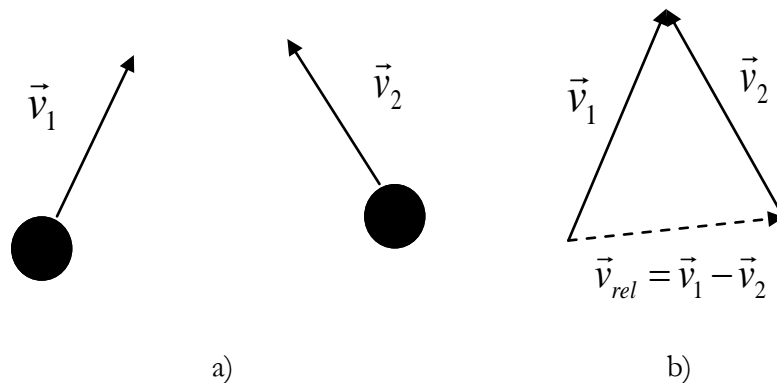


Figure 20. a) Two atoms with corresponding velocities, 1 and 2. b) The relationship between the velocity vectors of the two atoms and the relative velocity between them.

As noted in the figure, vector subtraction relates the velocities of two different particles and the relative velocity between them. The magnitude of the relative velocity is therefore given by

$$v_{rel} = \sqrt{(\vec{v}_1 - \vec{v}_2) \cdot (\vec{v}_1 - \vec{v}_2)} = \sqrt{v_1^2 + v_2^2 - 2\vec{v}_1 \cdot \vec{v}_2}. \quad (7)$$

Because the directions of particle velocities are randomized over a large number of atoms, the cross term cancels. Due to this and the fact that the average velocity of all atoms is \bar{v} , the magnitude of the relative velocity simplifies to

$$v_{rel} = \sqrt{2}\bar{v}. \quad (8)$$

Therefore the frequency of collisions from Equation (6) becomes

$$\frac{N}{V} \pi d^2 \sqrt{2} \bar{v} dt. \quad (9)$$

Dividing the length of the path from Equation (3), by the frequency of collisions, the average distance between collisions is shown to be

$$\lambda = \frac{V}{\sqrt{2} N \pi d^2}. \quad (10)$$

Assuming the atoms behave like an ideal gas where k is Boltzmann's constant, N is the total number of atoms, T is the temperature, and P is the pressure, the mean free path is

$$\lambda = \frac{kT}{\sqrt{2} P \pi d^2}. \quad (11)$$

Notice that the relationship is inversely proportional to the pressure. Therefore as the pressure in the deposition chamber decreases, it becomes less likely that an atom will collide with residual gas molecules over the distance between the source and the substrate.

After having derived a relationship for the mean free path, a ratio that qualitatively describes the interactions between molecules in low pressure systems can be determined [41]. The Knudsen

number K_n is used to differentiate between molecular flow ($K_n > 1$) and fluid flow ($K_n < 0.01$). The former is characterized by molecules moving independently of each other and collisions with walls being more common than those with other molecules, while the latter is just the opposite. The Knudsen number is defined as

$$K_n = \frac{\lambda}{l}. \quad (12)$$

In this relationship l is the characteristic dimension of constraint for the process being considered. For example, in determining the ratio for metal atoms travelling between the evaporation source and the substrate, l is the distance between the source and the walls of the chamber. Notice that having a high Knudsen number is as important as having a long mean free path for both contamination and diffusion of the evaporated metals during the deposition process.

3.2 Evaporation Theory

Evaporation for producing thin metal films is accomplished by a variety of means as discussed in Section 2.2. It is important to introduce evaporation theory to better understand the physical properties controlling this process. In doing so, an expression for the evaporation rate can be derived to obtain initial estimates of the rate versus temperature for thickness monitoring (Section 2.3.2). Central to an introduction of evaporation theory is the Hertz-Knudsen equation. From kinetic theory, Gustav Hertz derived the following relationship for the evaporation rate of materials [42]. It can be shown that the flux, the number of atoms incident on an area per unit time, is given by [43]

$$F = \frac{1}{4} n \bar{v}. \quad (13)$$

In this relationship, n is the number of molecules per unit volume and \bar{v} is their average velocity. If the gas is assumed to be ideal, n can be written as

$$n = \frac{p}{kT}, \quad (14)$$

where p is the pressure of the gas, T its temperature, and k is Boltzmann's constant. Therefore, combining Equation (13) and Equation (14), the flux is

$$F = \frac{p\bar{v}}{4kT}. \quad (15)$$

This relationship can be completed by determining an expression for the average velocity. Classically, the velocity of any one molecule in a group of N total can range from zero to infinity. If ΔN_i is the number of molecules with velocity v_i , their average velocity is given by

$$\bar{v} = \frac{1}{N} \sum_{i=0}^{\infty} v_i \Delta N_i \approx \frac{1}{N} \int_0^{\infty} v \frac{dN}{dv} dv. \quad (16)$$

Assuming a Maxwell-Boltzmann distribution of velocities, the number of molecules ΔN within a velocity range Δv is [44]

$$\frac{\Delta N}{\Delta v} = \frac{4N}{\sqrt{\pi}v_m^3} v^2 \exp\left(-\frac{v^2}{v_m^2}\right) \approx \frac{dN}{dv} \quad (17)$$

where v_m is a function of the molecular mass m , the temperature T , and includes Boltzmann's constant k . It is defined as

$$v_m = \sqrt{\frac{2kT}{m}}. \quad (18)$$

Substituting Equation (17) into Equation (16), the average velocity is approximated to be

$$\bar{v} = \frac{4}{\sqrt{\pi}v_m^3} \int_0^{\infty} v^3 \exp\left(-\frac{v^2}{v_m^2}\right) dv = \sqrt{\frac{8kT}{m\pi}}. \quad (19)$$

Combining the result of Equation (19) with that of Equation (15), the flux is shown as

$$F = \frac{p}{\sqrt{2\pi mkT}}. \quad (20)$$

As depicted in Figure 21, when a material and its vapor are isolated in a container, the flux of the solid or liquid phase will be incident on the vapor phase and vice versa. If the atomic flux from the material onto the vapor is higher, more atoms will be entering the vapor phase. Therefore the difference between the fluxes yields this rate of evaporation. Assuming thermal equilibrium, a molecular mass m , a vapor pressure p^* for the material, and a pressure p for the vapor, the evaporation rate is [42]

$$\Delta F = \frac{dN}{A dt} = (2\pi m k T)^{-\frac{1}{2}}(p^* - p). \quad (21)$$

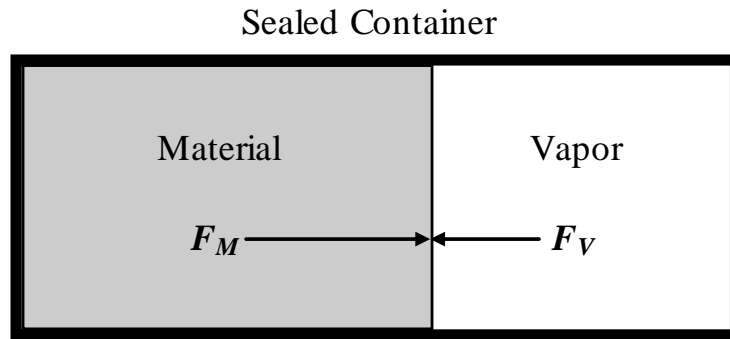


Figure 21. A solid or liquid material and its vapor in a sealed container. The evaporation rate of the material is given by the difference between the atomic fluxes F_M and F_V that are impinging on the other phase.

Equation (21) is referred to as the Hertz equation and is written in terms of the interface area A , and the rate at which atoms leave the material, dN/dt . Notice that the assumption has been made that the vapor phase is at a constant pressure throughout. Also, notice that as the pressure of the vapor phase approaches zero, the evaporation rate approaches a theoretical maximum. Because nearly all atoms leaving the metal will not return, this is an acceptable approximation for evaporation under high vacuum.

To test his theory, Hertz vaporized mercury under vacuum, making this same approximation. His results however, showed much lower rates than predicted. Knudsen attributed this to atoms that added to the pressure of the gas phase, but upon impingement on the mercury, were reflected from the surface and not reabsorbed, resulting in a decrease of the rate. He adjusted the relationship by adding the empirically-determined evaporation coefficient α_v . The common representation of the Hertz-Knudsen equation is

$$\frac{dN}{Adt} = \alpha_v(2\pi mkT)^{-\frac{1}{2}}(p^* - p). \quad (22)$$

The maximum theoretical evaporation rate is then

$$\frac{dN}{Adt} = \frac{\alpha_v p^*}{\sqrt{2\pi mkT}}. \quad (23)$$

Notice that this does not give the full relationship between the evaporation rate and the temperature because the vapor pressure is also a function of T . If however, the vapor pressure at a given temperature is known, Equation (23) can be used to predict the rate of evaporation for different materials.

For use with the apparatus presented in Chapter 4 and Chapter 5 specifically, a relationship can be determined for approximating the deposition rate. Consider the situation shown in Figure 22. In this diagram, the source is approximated as a hemisphere of area A_e , emitting the evaporant flux equally in all directions. This approximation yields a conservative estimate because in actuality, the crucible will further limit the direction of the flux. Included in the path of the evaporated atoms is a substrate of area A_s , at a distance r from the source.

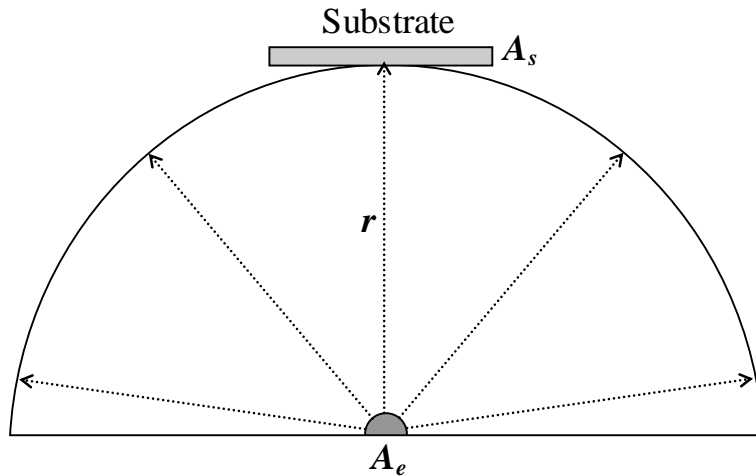


Figure 22. Evaporation from a hemispherical source of area A_e , covering a hemisphere of radius r . Part of this hemisphere includes the substrate of area A_s .

The ratio of the evaporant leaving the source to that of the evaporant arriving at the substrate is given by the ratio of their solid angles. The solid angle for the hemisphere is 2π and for the substrate is given by

$$d\Omega = \frac{dA_s}{r^2} \approx \frac{A_s}{r^2}. \quad (24)$$

For the case illustrated here, the assumption is made that the radius is constant over the area of the substrate. This is a good approximation for large radii and comparatively small substrates, as is the situation here. As a result, the percent of the flux that is incident on the substrate F_s , is

$$F_s = \frac{A_s}{2\pi r^2}. \quad (25)$$

Recall that the evaporation rate for this situation is given from Equation (23), where A is the area of the evaporating surface, A_e . Therefore, the rate per unit area at the substrate is given by the rate at the source, multiplied by the percent flux that makes it to the substrate from Equation (25)

$$\frac{dN}{A_s dt} = \frac{A_e}{A_s} \frac{dN}{A_e dt} F_s = \frac{A_e p^*}{2\pi r^2 \sqrt{2\pi m k T}}. \quad (26)$$

Notice that the evaporation coefficient is assumed to be one. The deposition rate, the rate of thickness change dD/dt , is found by multiplying Equation (26) by the volume per atom of deposit. This is determined by dividing the atomic mass by the density of the film, ρ

$$\frac{dD}{dt} = \frac{A_e p^*}{2\pi \rho r^2} \sqrt{\frac{m}{2\pi k T}}. \quad (27)$$

Equation (27) assumes that all atoms are adsorbed to the growing film and the distribution is uniform. For thickness uniformity considerations, see Section 3.3.

As an example, the rate for silver is predicted using values of the vapor pressure at given temperatures obtained from Ref. [45]. These values and the resulting deposition rate from Equation (27) are shown

in Table 1 and are plotted in Figure 23. These results allow for a prediction of the deposition rate at a given temperature which can be used as an initial calibration for temperature rate monitoring.

Table 1. Tabulated results for the vapor pressure at given temperatures for silver. The deposition rate is approximated using the indicated relationship. Vapor pressure and temperature measurements taken from Ref. [45].

Temperature (K)	Vapor Pressure (Torr)	Vapor Pressure (Pa)	Deposition Rate (nm/s)
1195 ± 5	$1.0 \times 10^{-3} \pm 20\%$	$1.3 \times 10^{-1} \pm 20\%$	$(4.6 \pm 1) \times 10^{-4}$
1300 ± 5	$1.0 \times 10^{-2} \pm 20\%$	$1.3 \pm 20\%$	$(4.4 \pm 0.9) \times 10^{-3}$
1435 ± 5	$0.10 \pm 20\%$	$13 \pm 20\%$	$(4.2 \pm 0.9) \times 10^{-2}$
1605 ± 5	$1.0 \pm 20\%$	$1.3 \times 10^2 \pm 20\%$	$(4.0 \pm 0.8) \times 10^{-1}$
1815 ± 5	$10 \pm 20\%$	$1.3 \times 10^3 \pm 20\%$	3.7 ± 0.8
2100 ± 10	$1.0 \times 10^2 \pm 20\%$	$1.3 \times 10^4 \pm 20\%$	35 ± 7

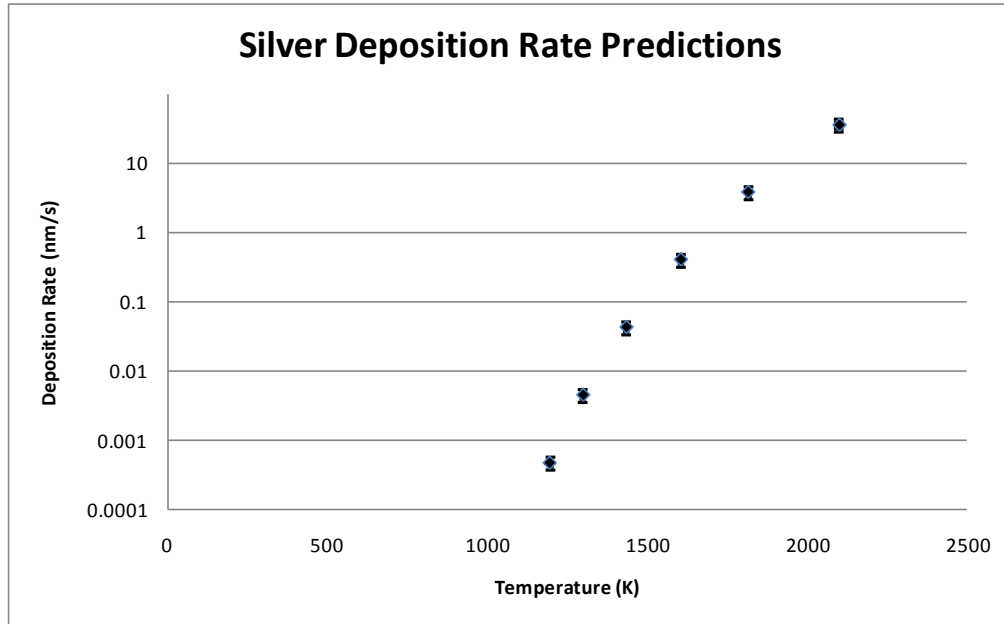


Figure 23. Predicted rates for the deposition rate versus the temperature for silver. The deposition rate is plotted on a logarithmic scale.

For these approximations, the area of the evaporation surface was estimated at 1cm^2 , the radius as $(76 \pm 3) \text{ cm}$, and the density for pure silver, 10.5 g/cm^3 was assumed. Uncertainty was included for the radius because the exact placements of the substrate and source have not been decided upon. For calculating the uncertainty in the final deposition rate, the relationship for the propagation of uncertainty was used

$$\delta f^2(x_1, x_2, \dots, x_n) = \sum_{i=0}^n \left(\frac{\partial f}{\partial x_i} \right)^2 \delta x_i^2. \quad (28)$$

In this equation, the uncertainty δf for a function f , is calculated from the uncertainty for each variable x_i , with uncertainty, δx_i . Using Equation (28) and the uncertainties for the vapor pressure, radius, and temperature, the uncertainty for the deposition rate simplifies to

$$\delta \left(\frac{dD}{dt} \right) = \frac{dD}{dt} \sqrt{\left(\frac{\delta p^*}{p^*} \right)^2 + \left(\frac{4\delta r^2}{r^2} \right) + \left(\frac{\delta T^2}{4T^2} \right)}. \quad (29)$$

3.3 Thickness Distribution

Notice that, from purely geometric arguments, the distribution of the film may not be consistent over a given area. An approximation for the amount of material deposited at a given location may be found in Ref. [46]. As depicted in Figure 24, the amount of material deposited, dm_d per unit area dA , is given by the mass of the material emitted from the source m_e , divided by the surface area of a sphere of radius r

$$\frac{dm_d}{dA} = \frac{m_e}{4\pi r^2}. \quad (30)$$

If the collecting surface is not perpendicular to the radial line as assumed in Equation (30) and shown in Figure 24, Equation (30) becomes

$$\frac{dm_d}{dA} = \frac{m_e}{4\pi r^2} \cos\theta. \quad (31)$$

Notice then that the thickness for a film of density ρ is given by

$$D = \frac{1}{\rho} \frac{dm_d}{dA}. \quad (32)$$

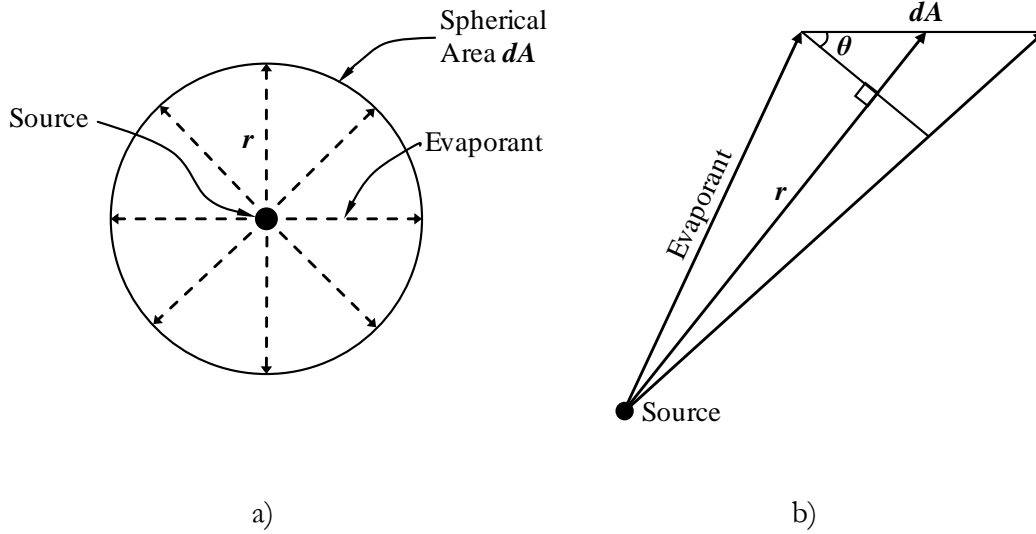


Figure 24. a) Metal evaporating from a point source onto a region dA from a distance r . b) Evaporant incident on dA at an angle instead of normal to the surface as in a).

As a result, the thickness D from Equation (32) is

$$D = \frac{1}{\rho} \frac{m_e}{4\pi r^2} \cos\theta . \quad (33)$$

Notice that the thickness distribution of a film on a flat substrate will not be uniform over the substrate area but will theoretically follow a cosine distribution as established in Equation (33). Abnormalities in the flux can cause it to follow a different distribution experimentally but there will be an angular dependence on the thickness. It is important to note that the smaller the angle of displacement from the normal, the less thickness variation there is across a given area.

DESCRIPTION OF APPARATUS

4.1 Overview

A drawing of the deposition chamber that is being designed and built at Houghton College is shown in Figure 25. Scale drawings and descriptions of individual components are featured in the following sections of this chapter.

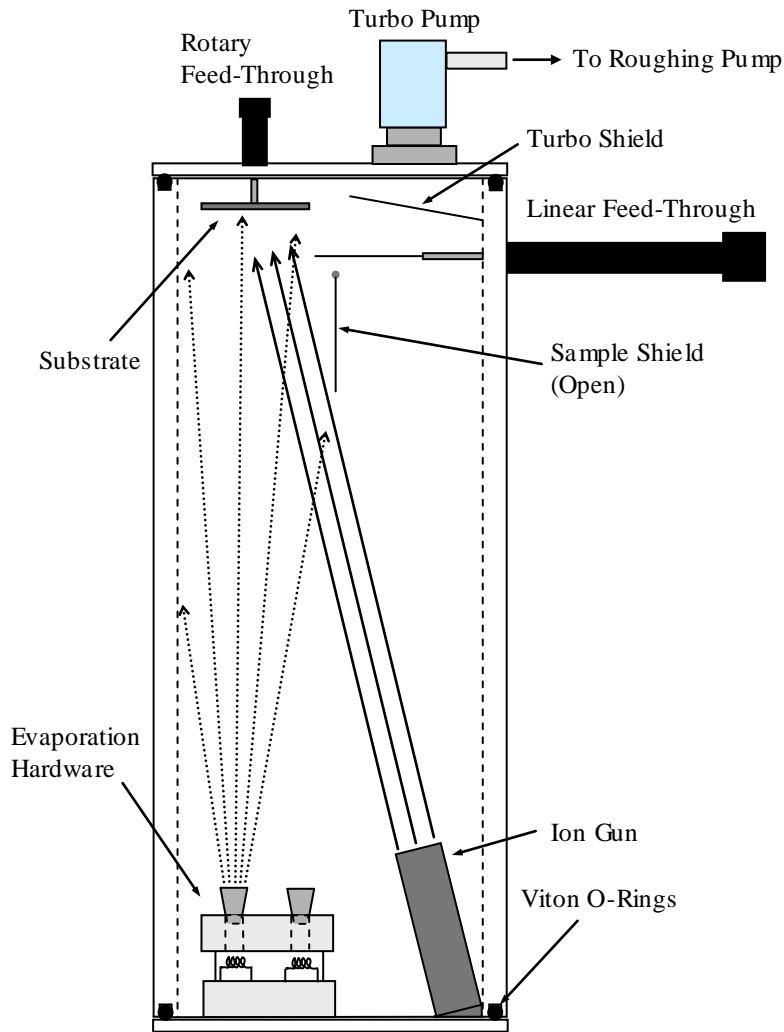


Figure 25. Overview diagram of the Houghton College deposition chamber, illustrating the important features and their approximate locations.

The deposition chamber is made of an aluminum cylindrical body, top, and bottom, and is sealed using Viton o-rings. An oil-sealed rotary pump reduces the chamber pressure initially, before a turbomolecular pump is used for further evacuation. Metals will be evaporated at the bottom of the chamber with the evaporant travelling upwards before adsorbing to the substrate at the top. The substrate is mounted to a rotary feedthrough, enabling rotational motion during deposition. This yields a more even distribution of the evaporated atoms on the substrate, producing a more uniform film thickness. An ion gun is also aimed to direct a beam of energetic ions at the substrate, for IBAD studies.

A variety of shields have also been added to the deposition chamber design. A sample shield is mounted to the end of a rotary feedthrough so that the evaporated flux or ions can be blocked from the substrate when necessary. Also, these are blocked from the inlet to the turbomolecular pump by a permanent shield. Because turbo pump rotors spin at high RPMs, any materials that could destroy the delicate balance required by the rotor cannot be allowed to enter the inlet. Lastly, a third shield is included for the deposition of samples with differences in film thickness across the substrate, making multiple thickness samples at once. This shield is mounted to a linear feedthrough that can be moved back and forth by a computer. Therefore, the shield can be precisely positioned, blocking portions of the substrate from the evaporated flux during deposition.

A general diagram of the evaporation hardware is shown in Figure 26. It is constructed of two ceramic blocks, separated by ceramic columns. These blocks insulate the various components and the chamber both electrically and thermally. The top ceramic block has four holes that graphite crucibles are placed in. Beneath each hole is a tungsten filament supported by a cylindrical molybdenum shield. To create an electric field between the filament and crucible, the crucible is held at ground while the filament is held at a negative potential, as is the molybdenum shield. This shield blocks electrons emitted in any direction but upward and also blocks radiation emitted from the hot filament. A current flows through the filament causing the thermionic emission of electrons. Any electrons emitted upwards will travel through the electric field between the crucible and the tantalum shield, accelerating them towards the base of the crucible. This energetic bombardment heats the crucible, and, as a result, the metal inside, causing its evaporation.

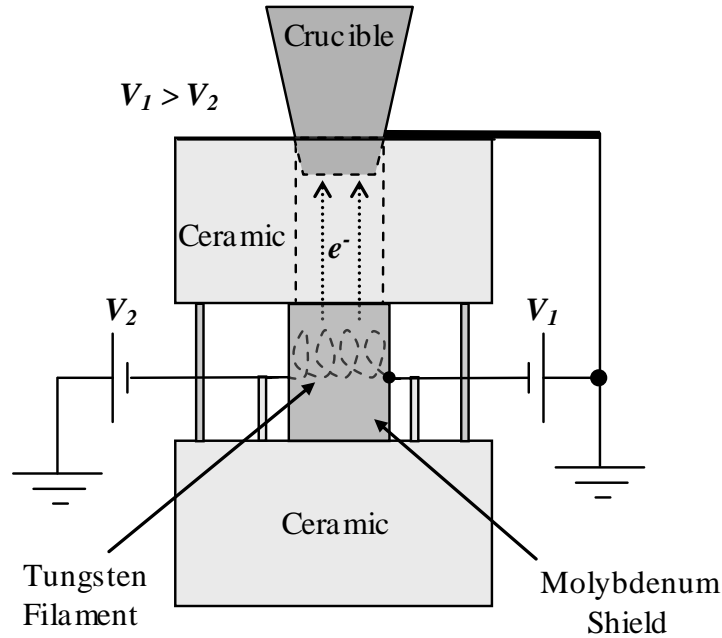


Figure 26. Diagram of the evaporation hardware that will be used to evaporate the metal to be deposited.

4.2 Top and Bottom

The chamber top and bottom are both made of $\frac{1}{2}$ inch aluminum and were ordered as 12 inch diameters. Their scale drawings are presented in Figure 27 and Figure 28 respectively. Both feature 36 holes at an outer radius through which screws pass, securing them to the body of the chamber. A rotary table mounted to a mill was used to drill holes through the top, whereas the bottom was drilled while mounted to the body of the chamber which was mounted to a rotary table. This was accomplished using a drill press. Both allowed placement of the holes every 10° .

The top of the chamber also features large holes for the turbomolecular pump and for the substrate to pass through. In order to cut these out, the center of each desired hole was first drilled out using a small drill bit so that the top could be bolted to a rotary table. An end mill was then used to remove material at the specified radius until the top was separated from the inside material.

The tapped holes that secure the turbomolecular pump and the substrate mounting plate to the top were drilled using a rotary table on a mill. For the pump hole, the 5/16-24 tapped holes are used to secure the turbomolecular pump whereas the 6-32 holes surrounding the substrate hole secure the

substrate mounting plate to the top. Each provides enough room between the center hole and the tapped holes for a Viton o-ring to seal the joint between them.

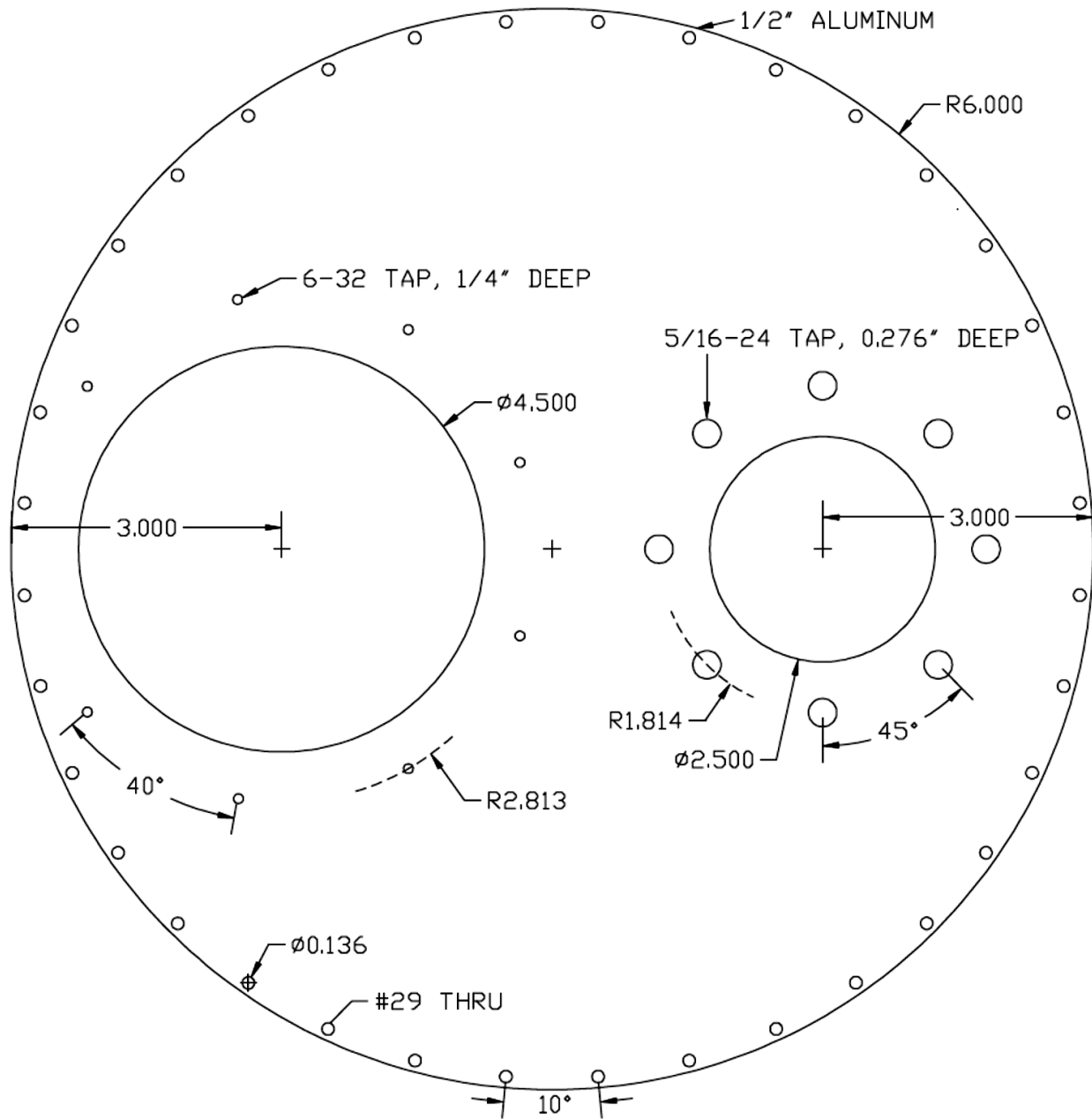


Figure 27. Scale drawing of the top of the chamber. Top has 36 holes on the outside to secure it to body, a large hole for the substrate mounting plate (left), and a large hole for the turbomolecular pump (right). Dimensions in inches.

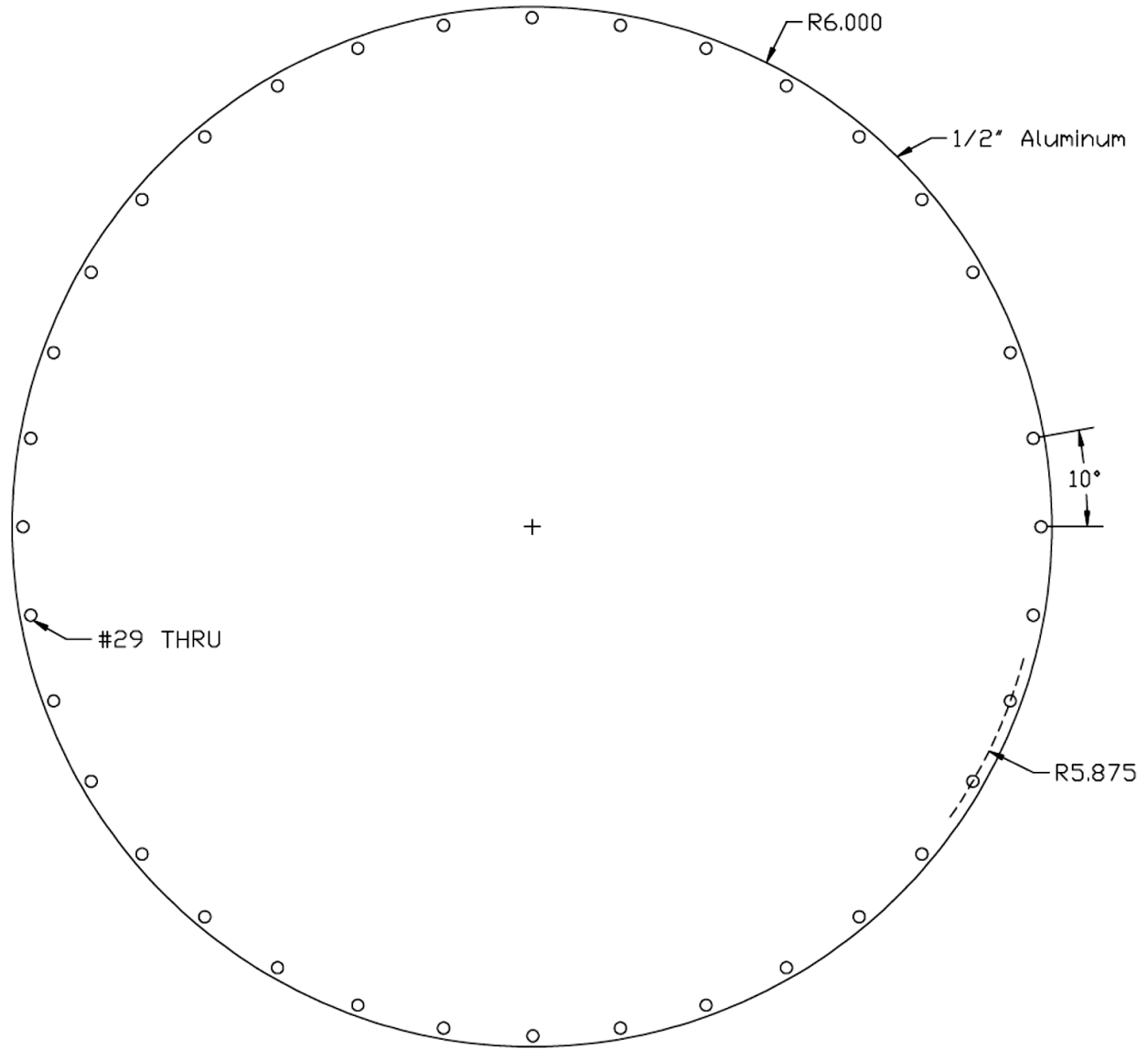


Figure 28. Scale drawing of the bottom of the chamber, featuring 36 holes to secure the bottom to the body of the chamber. Dimensions in inches.

4.3 Substrate Mounting Plate

The substrate mounting plate, shown in Figure 29, supports the substrate and allows for the easy changing of samples. By removing this plate, the substrate can be separated from the chamber without having to remove the top. The plate was cut from a 3/8 inch thick piece of aluminum using the lathe. First, a 1/4 inch hole was drilled through the center and the piece was attached to the lathe through this hole. The plate was then turned down to 6 inches in diameter before facing each side. A lathe was

used to make an o-ring channel for sealing the substrate mounting plate to the top of the chamber. The lathe was used specifically so that all marks in the channel were circumferential. Any radial defects can be a source for small leaks. The channel was made 0.248 inches wide at a depth of 0.151 inches to accept an o-ring with a cross section diameter of 0.210 ± 0.005 inches. This was made wider than the width of the lathe tool because if the channel is cut too narrow, the tool can vibrate, producing radial marks. The center hole was then widened using a size Q drill bit.

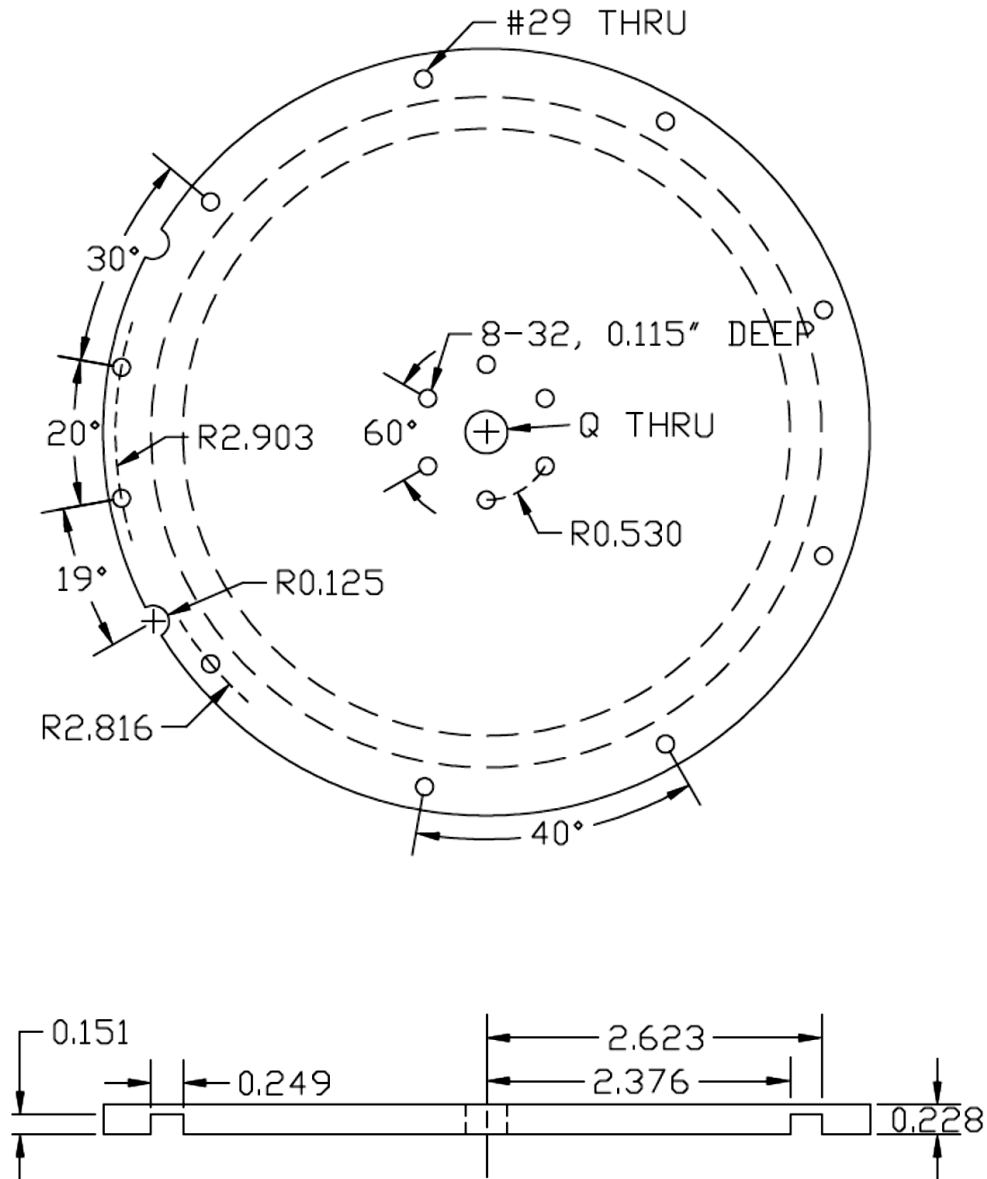


Figure 29. Scale drawings of top and side of substrate mounting plate. Hidden lines for screw holes (except the center one) and two cut radii are not included in the side view. All dimensions in inches.

Next, the mounting plate was attached to a rotary table and the remaining holes were drilled on a mill. At a radius of 2.816 inches, 8 holes were drilled 40° apart to mount the plate to the top using screws. To further secure the substrate mounting plate to the top, two holes were drilled at a radius of 2.903 inches and were placed 20° apart. These holes were designed to line up with the holes at the outside of the top. This allows 6-32 screws to pass through the substrate mounting plate, through the top, and then into the tapped holes in the body of the chamber. Also, six holes were drilled at a radius of 0.53 inches and were tapped for 8-32 screws. This is where the rotary feedthrough is mounted to the substrate mounting plate. This rotary feedthrough directly supports the substrate inside the chamber.

Lastly, two 1/8 inch radii were cut 19° from the holes aligning with the holes in the top plate. These were necessary to provide space for the next set of screws for securing the top plate to the body of the chamber.

4.4 Body

The body of the chamber is made of a cylindrical piece of aluminum that is 3 feet tall and a half inch thick with an outer diameter of 12 inches. Scale drawings for the top, side, and feedthrough holes are shown in Figure 30, Figure 31 and Figure 32 respectively. The height of the body ensures that the metal atoms will strike the substrate at normal incidences with a variation of less than 4°, producing a thickness variation of less than 1% (see Section 3.3). On both the top and the bottom of the body, 36 holes were drilled and tapped to accept 6-32 screws and secure the top and bottom plates to the body of the chamber. Also, on both top and bottom of the body, o-ring channels were cut on the lathe. These were made to accept o-rings with a cross section diameter of 0.139 ± 0.004 inches and have a width of 0.160 inches and depth of 0.101 inches.

On the side of the body as shown in Figure 30 and Figure 31, portions were flattened with an end-mill so that various feedthroughs could be added to the side of the chamber. After the areas were flattened, 6 holes were drilled to a depth of 0.23 inches 60° apart and were tapped for 1/4-20 bolts for 2.75 inch feedthroughs and 6-32 bolts for 1.333 inch feedthroughs. After all machining was completed, the flattened portion was smoothed further using 600 grit sandpaper, followed by 1 micron diamond paste.

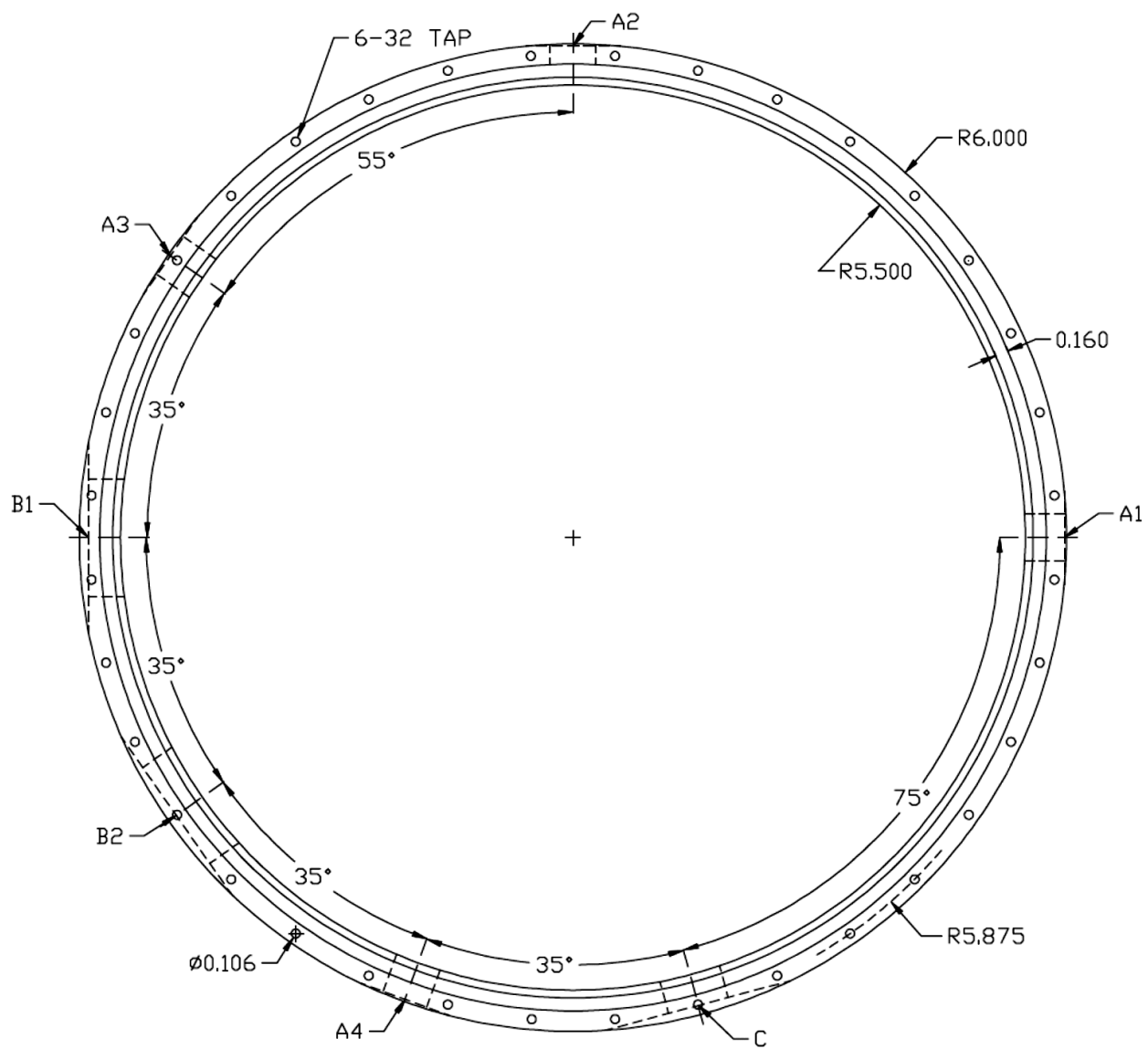


Figure 30. Scale drawing top view of body. Cylindrical aluminum tube with 36 tapped holes and o-ring channels on top and bottom. Holes are used to attach chamber top and bottom to body. A1-A4, B1-B2, and C indicate positions of feedthroughs. Dimensions are given in Figure 32. Dimensions in inches.

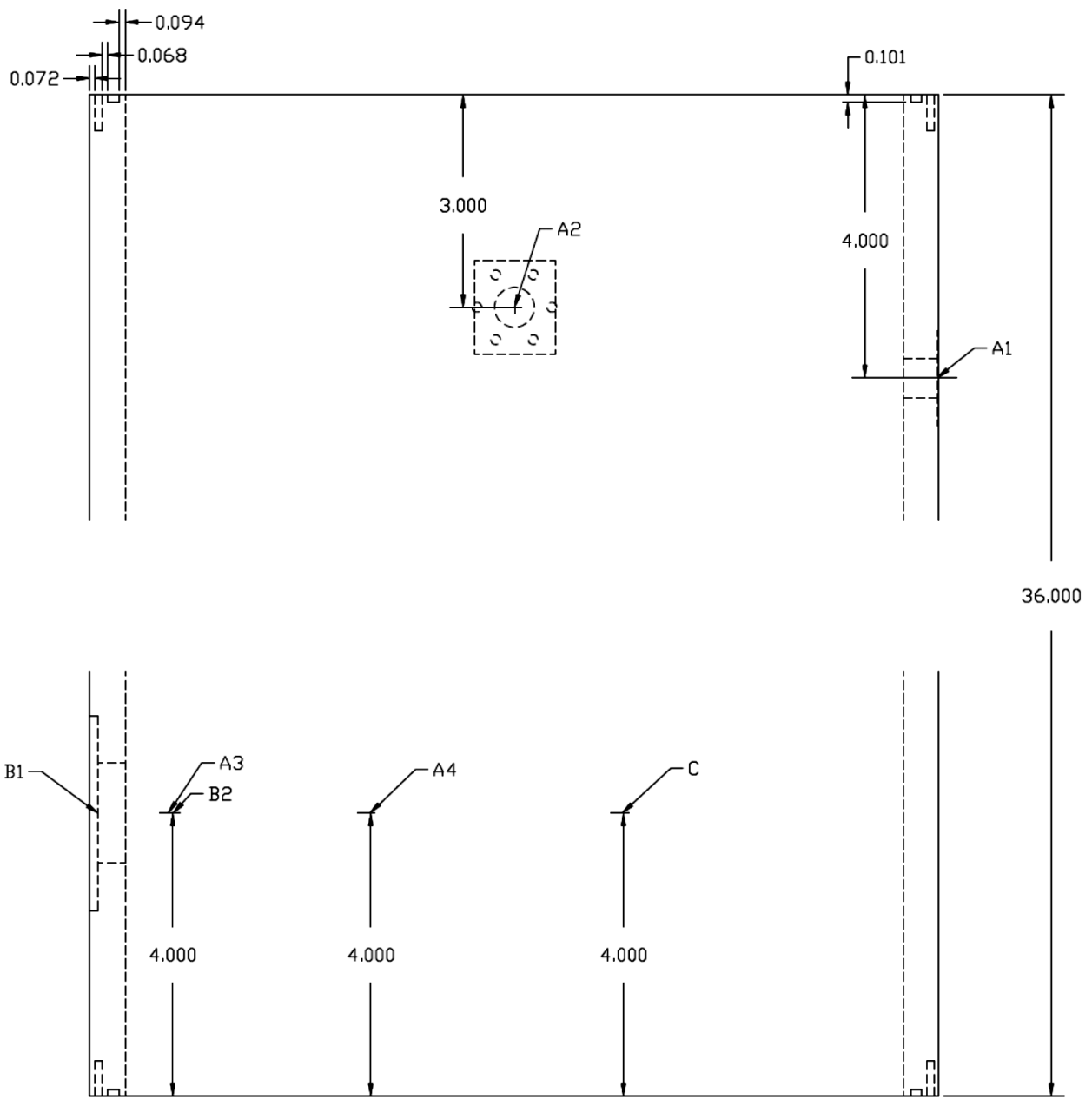


Figure 31. Scale drawing side view of body. Locations of A3-A4, B1-B2, and C are specified by angular location in Figure 30. Dimensions in inches.

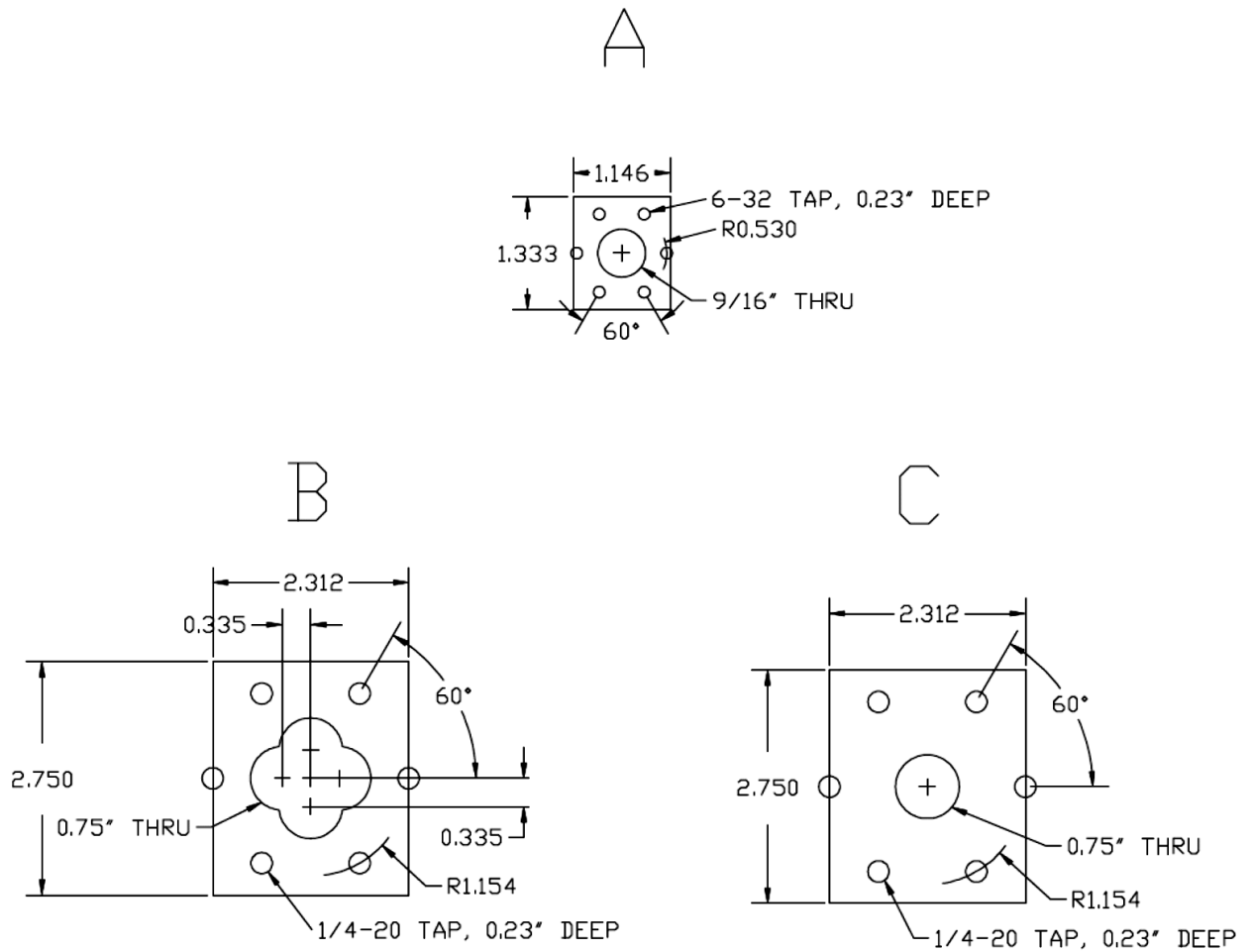


Figure 32. Specifications for A1-A4, B1-B2, and C – A, B, and C respectively. Rectangle indicates size of flattened area on side of body. Locations shown in previous drawings indicate location of center for A, B, or C. Figures drawn as they would appear viewed head on, on side of body. Dimensions in inches.

RESULTS AND CONCLUSIONS

5.1 Initial Results

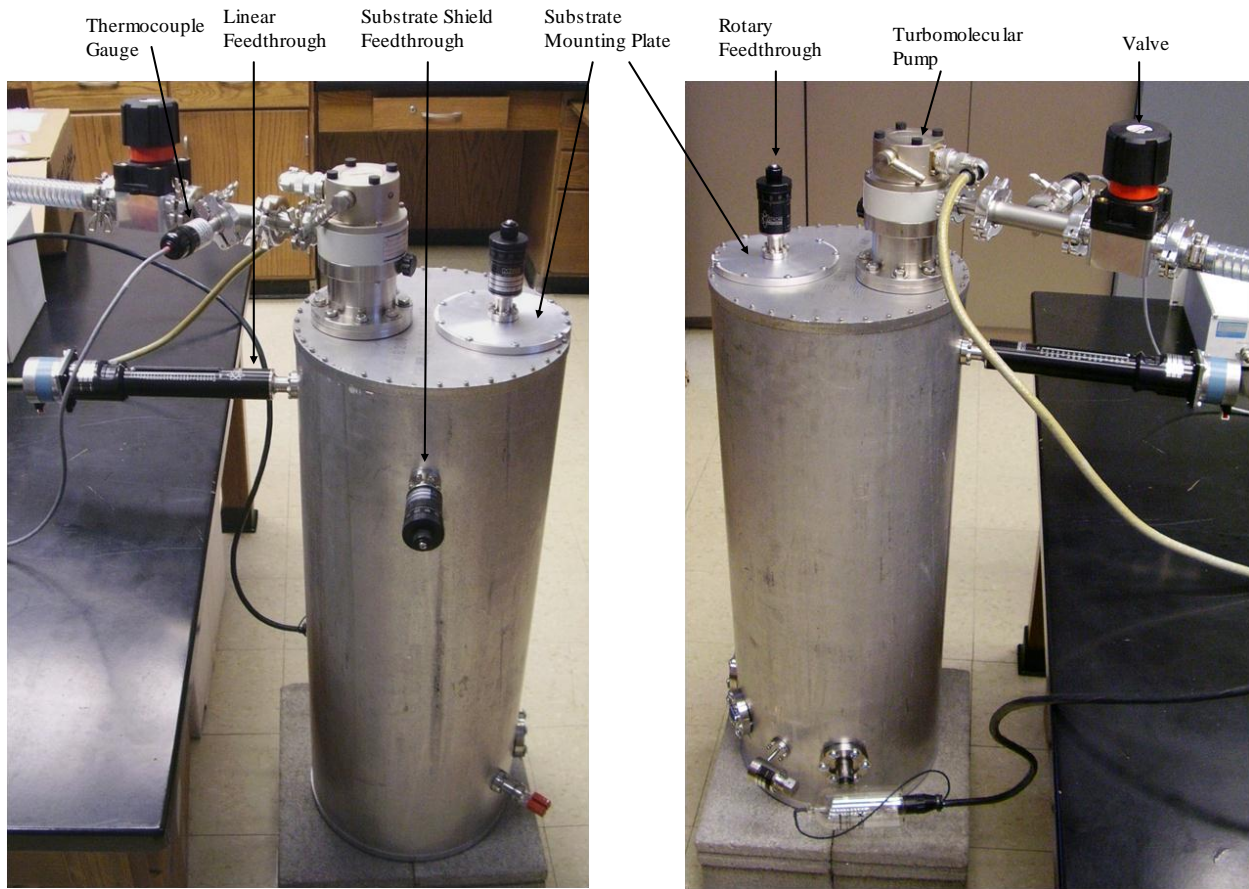
The components that have been drafted and discussed in the previous chapter have been machined and put together to form the vacuum chamber. All aluminum components were made from 6061 extruded aluminum obtained from Pierce Aluminum Company. As shown in Figure 33, two MDC BRM-133 rotary feedthroughs, an MDC MLV-22 needle valve, a thermocouple (Kurt J. Lesker TFT2CY00002), and two electrical feedthroughs (Kurt J. Lesker IFTRG107013 and IFDGG091053) have been added to the chamber. Viton gaskets (VG-133, VG-275, and VG-450) from the Duniway Stockroom Corporation are used with each feedthrough to provide a seal between the conflat flange and the chamber. To seal the top and bottom to the body of the chamber, V1000-276 Viton o-rings from Marco Rubber are used and a V1000-350 Viton o-ring is used for the substrate mounting plate. An Alcatel M2008A two-stage rotary pump is used to back a Pfeiffer TPU060 turbomolecular pump.



Figure 33. View of installed feedthroughs at bottom of deposition chamber.

To measure the pressure of the system, a thermocouple gauge (Kurt J. Lesker KJL 6000-QF16) has been installed between the rotary and turbomolecular pump and a Duniway Stockroom I-100-K ion gauge has been mounted on the side of the chamber. A Granville-Phillips 280 Gauge Controller controls the thermocouple gauge and a Stanford Research Systems IGC100 controls the ion gauge.

The top, bottom, and body of the chamber were initially cleaned using water and Spartan “Clean by Peroxy” hydrogen peroxide based cleaner. This step removed oil, shavings, and other grime resulting from the machining process. This was followed by a cleaning of all surfaces in contact with the high vacuum using methanol and kim wipes. This included all feedthroughs and Viton o-rings.



a)

b)

Figure 34. Front (a) and back (b) view of deposition chamber with top components labeled.

After everything was secured using the correctly sized screws and bolts, the rotary pump was started and allowed to run for approximately 5 minutes before starting the turbomolecular pump. At this time, the thermocouple gauge measured a pressure of approximately 10^{-2} torr. About 5 to 10 minutes after starting the turbomolecular pump, the rotor was at full speed and the pressure was measured by the ion gauge to be in the 10^{-6} torr range. Two fans were placed blowing air onto the turbomolecular pump to keep it cool. Currently, after the turbomolecular pump has been running for approximately one week, a base pressure of 3×10^{-7} torr has been measured.

5.2 Future Work

In the near future, the chamber will be baked at a temperature of 150°C for a period of a couple days. This will increase the rate of desorption from the chamber walls and as a result, lower the base pressure that can be attained in this time period.

To date, the vacuum chamber is the only part of the system that has been both fully designed and constructed. All shields inside the chamber are yet to be designed and their exact placements decided upon. The effect that the turbomolecular pump shield has on the pumping speed will be closely examined during this portion of the design. The ionization rate monitoring device will be designed and constructed similar to the one used by Giedd and Perkins [31] but work has not begun on this component yet. The evaporation hardware is being designed and constructed by another student and will be completed soon. Lastly, an ion gun is yet to be designed and constructed and may be purchased depending on the rate of progress.

After everything has been constructed or purchased, a layout for the system will be decided upon and everything will be put in place. Soon afterwards, the ability to produce thin metal films at Houghton College will be attained and these films and their microstructures will be studied to determine the effects that different deposition variables have on the resulting film.

References

-
- [1] W. R. Grove, Phil. Trans. B, **142**, 87 (1852).
 - [2] M. Faraday, Phil. Trans., **147**, 145 (1857).
 - [3] A. W. Wright, Amer. J. Sci. and Arts, **13**, 49 (1877).
 - [4] T. A. Edison, U. S. Patent No. 484,582 (18 October, 1892).
 - [5] T. A. Edison, U. S. Patent No. 488,189 (20 December, 1892).
 - [6] T. A. Edison, U. S. Patent No. 680,520 (13 August, 1901).
 - [7] T. A. Edison, U. S. Patent No. 767,216 (9 August, 1904).
 - [8] J. M. Lafferty, Phys. Today, **34** (11), 211 (1981).
 - [9] Y. Tito Sasaki, J. Vac. Sci. Technol. A, **9** (3), 2025 (1991).
 - [10] N. Kaufherr, A. Krauss, D. M. Gruen, R. Nielsen, J. Vac. Sci. Technol. A, **8** (3), 2849 (1990).
 - [11] A. Berman, Vacuum, **47** (4), 327 (1996).
 - [12] R. W. Roberts, L. E. St. Pierre, Sci. New Series, **147** (3665), 1529 (1965).
 - [13] Y. Nagamitsu, J. Vac. Sci. Technol. A, **7** (1), 110 (1989).
 - [14] S. Dushman, *Production and Measurement of High Vacuum*. (General Electric Review, Schenectady, New York, 1922), p. 51-52.
 - [15] H. G. Tompkins, T. A. Gessert, *Pumps Used in Technology*. (American Vacuum Society, New York, 2001), p. 1-91.
 - [16] S. Dushman, *Scientific Foundation of Vacuum Technique*. (John Wiley & Sons, Inc., New York, 1955), p. 313-315.
 - [17] G. C. Dunlap, J. G. Trump, Rev. Sci. Instr., **8**, 37 (1937).
 - [18] S. Dushman, *Scientific Foundations of Vacuum Technique*. (John Wiley & Sons, Inc., New York, 1955), p.332-333.
 - [19] R. T. Bayard, D. Alpert, Rev. Sci. Instr., **21** (6), 571 (1950).
 - [20] D. M. Mattox, *Handbook of Physical Vapor Deposition (PVD) Processing*. (Noyes Publications, Park Ridge, New Jersey, 1998), p. 315.
 - [21] D. M. Mattox, *Handbook of Physical Vapor Deposition (PVD) Processing*. (Noyes Publications, Park Ridge, New Jersey, 1998), p. 269.
 - [22] J. Strong, Phys. Rev., **39**, 1012 (1932).
 - [23] C. H. Cartwright, J. Strong, Rev. Sci. Instr., **2**, 189 (1931).

-
- [24] W. C. Caldwell, J. Appl. Phys., **12**, 779 (1941).
- [25] E. B. Graper, J. Vac. Sci. Technol. A, **5** (4), 2718 (1987).
- [26] F. L. Schuermeyer, W. R. Chase, E. L. King, J. Vac. Sci. Technol., **9** (1), 330 (1972).
- [27] H. M. O'Bryan, Rev. Sci. Instrum., **5** (3), 125 (1934).
- [28] I. Langmuir, Proc. Natl. Acad. Sci., Wash., **3** (3), 141 (1917).
- [29] D. W. Pashley, M. J. Stowell, M. H. Jacobs, T. J. Law, Phil. Mag., **10** (103), 127 (1964).
- [30] L. I. Maissel, R. Glang, *Handbook of Thin Film Technology*. (McGraw-Hill Book Company, New York, 1970), p.107.
- [31] G. R. Giedd, M. H. Perkins, Rev. Sci. Instr., **31** (7), 773 (1960).
- [32] P. Atkins, J. De Paula, *Atkins' Physical Chemistry*. (Oxford University Press, New York, 2006), p.697-701.
- [33] J. S. Colligon, Phil. Trans., **362** (1814), 103 (2004).
- [34] I. Petrov, P. B. Barna, L. Hultman, J. E. Greene, J. Vac. Sci. Technol. A, **21** (5), S117 (2003).
- [35] D. W. Pashley, Adv. Phys., **5** (18), 173, (1956).
- [36] L. Holland, J. Opt. Soc. Am., **43** (5), 376 (1953).
- [37] H. Ji, G. S. Was, J. W. Jones, N. R. Moody, J. Appl. Phys., **81** (10), 6754 (1997).
- [38] B. Little, Unpublished, (2007).
- [39] C. V. Thompson, R. Carel, Mat. Sci. Eng. B, **32**, 211 (1995).
- [40] L. I. Maissel, R. Glang, *Handbook of Thin Film Technology*. (McGraw-Hill Book Company, New York, 1970), p. 21-2.
- [41] D. L. Smith, *Thin-Film Deposition*. (McGraw-Hill, New York, 1995), p. 25.
- [42] L. I. Maissel, R. Glang, *Handbook of Thin Film Technology*. (McGraw-Hill Book Company, New York, 1970), p.26.
- [43] F. W. Sears, G. L. Salinger, *Thermodynamics, Kinetic Theory, and Statistical Thermodynamics*. (Addison-Wesley Publishing Company, Phillipines, 1986), p. 251-257.
- [44] F. W. Sears, G. L. Salinger, *Thermodynamics, Kinetic Theory, and Statistical Thermodynamics*. (Addison-Wesley Publishing Company, Phillipines, 1986), p. 354-358.
- [45] R. E. Honig, RCA Review, **23**, 567 (1962).
- [46] L. I. Maissel, R. Glang, *Handbook of Thin Film Technology*. (McGraw-Hill Book Company, New York, 1970), p.36.